J. Fluid Mech. (2010), *vol.* 642, *pp.* 445–476.

doi:10.1017/S002211200999190X

Experimental and numerical investigation of turbulent convection in a rotating cylinder

R. P. J. KUNNEN[1]†, B. J. GEURTS[1,2] AND H. J. H. CLERCX[1,2]

[1]Fluid Dynamics Laboratory, Department of Physics, International Collaboration for Turbulence Research (ICTR) & J. M. Burgers Centre for Fluid Dynamics, Eindhoven University of Technology, PO Box 513, 5600 MB Eindhoven, The Netherlands

[2]Department of Applied Mathematics, International Collaboration for Turbulence Research (ICTR) & J. M. Burgers Centre for Fluid Dynamics, University of Twente, PO Box 217, 7500 AE Enschede, The Netherlands

(Received 2 April 2009; revised 31 August 2009; accepted 31 August 2009)

The effects of an axial rotation on the turbulent convective flow because of an adverse temperature gradient in a water-filled upright cylindrical vessel are investigated. Both direct numerical simulations and experiments applying stereoscopic particle image velocimetry are performed. The focus is on the gathering of turbulence statistics that describe the effects of rotation on turbulent Rayleigh–Bénard convection. Rotation is an important addition, which is relevant in many geophysical and astrophysical flow phenomena.

A constant Rayleigh number (dimensionless strength of the destabilizing temperature gradient) $Ra = 10^9$ and Prandtl number (describing the diffusive fluid properties) $\sigma = 6.4$ are applied. The rotation rate, given by the convective Rossby number Ro (ratio of buoyancy and Coriolis force), takes values in the range $0.045 \leqslant Ro \leqslant \infty$, i.e. between rotation-dominated flow and zero rotation. Generally, rotation attenuates the intensity of the turbulence and promotes the formation of slender vertical tube-like vortices rather than the global circulation cell observed without rotation. Above $Ro \approx 3$ there is hardly any effect of the rotation on the flow. The root-mean-square (r.m.s.) values of vertical velocity and vertical vorticity show an increase when Ro is lowered below $Ro \approx 3$, which may be an indication of the activation of the Ekman pumping mechanism in the boundary layers at the bottom and top plates. The r.m.s. fluctuations of horizontal and vertical velocity, in both experiment and simulation, decrease with decreasing Ro and show an approximate power-law behaviour of the shape $Ro^{0.2}$ in the range $0.1 \lesssim Ro \lesssim 2$. In the same Ro range the temperature r.m.s. fluctuations show an opposite trend, with an approximate negative power-law exponent $Ro^{-0.32}$. In this Rossby number range the r.m.s. vorticity has hardly any dependence on Ro, apart from an increase close to the plates for Ro approaching 0.1. Below $Ro \approx 0.1$ there is strong damping of turbulence by rotation, as the r.m.s. velocities and vorticities as well as the turbulent heat transfer are strongly diminished. The active Ekman boundary layers near the bottom and top plates cause a bias towards cyclonic vorticity in the flow, as is shown with probability density functions of vorticity. Rotation induces a correlation between vertical vorticity and vertical velocity close to the top and bottom plates: near the top plate downward velocity is correlated with positive/cyclonic vorticity and vice versa (close to the bottom plate upward velocity is correlated with positive vorticity), pointing to the

---

† Present address: Institute of Aerodynamics, RWTH Aachen University, Wüllnerstraße 5a, 52062 Aachen, Germany. Email address for correspondence: r.kunnen@aia.rwth-aachen.de

vortical plumes. In contrast with the well-mixed mean isothermal bulk of non-rotating convection, rotation causes a mean bulk temperature gradient. The viscous boundary layers scale as the theoretical Ekman and Stewartson layers with rotation, while the thermal boundary layer is unaffected by rotation. Rotation enhances differences in local anisotropy, quantified using the invariants of the anisotropy tensor: under rotation there is strong turbulence anisotropy in the centre, while near the plates a near-isotropic state is found.

Key words: Bénard, convection, rotating flows

1. Introduction

Rotating Rayleigh–Bénard convection is the flow in a layer of fluid enclosed by horizontal plates, driven by a destabilizing temperature gradient and modified by rotation. It can be concisely described with three dimensionless parameters:

$$Ra \equiv \frac{g\alpha\Delta T H^3}{\nu\kappa}, \quad \sigma \equiv \frac{\nu}{\kappa}, \quad Ta \equiv \left(\frac{2\Omega H^2}{\nu}\right)^2. \tag{1.1}$$

Here g is the gravitational acceleration, H the height of the fluid layer, ΔT the temperature difference applied between bottom and top plates and Ω the rotation rate; ν, κ and α are the kinematic viscosity, thermal diffusivity and thermal expansion coefficient of the fluid, respectively. A positive/counterclockwise rotation sense is assumed with the rotation vector aligned vertically, antiparallel with the gravitational acceleration. The Rayleigh number Ra represents the strength of the temperature gradient; the Prandtl number σ describes the diffusive properties of the fluid; and the Taylor number Ta is a dimensionless representation of the rotation rate. A convenient combination of these three parameters is the Rossby number

$$Ro \equiv \sqrt{\frac{Ra}{\sigma Ta}}, \tag{1.2}$$

which directly compares the buoyancy strength with the Coriolis force. The horizontally infinite layer is of course impossible in practical applications, and hence a lateral confinement is introduced. A popular geometry for experiments is an upright cylinder. The extra parameter to describe the geometry is the diameter-to-height aspect ratio $\Gamma \equiv D/H$, with D the diameter of the cylinder.

The addition of rotation to the Rayleigh–Bénard problem changes the stability criterion for onset of convection (Chandrasekhar 1961). The critical Rayleigh number for onset of convection, Ra_c, is increased when the Taylor number grows. Yet, the occurrence of a secondary instability, the so-called Küppers–Lortz instability (Küppers & Lortz 1969), enables the transition from steady to time-dependent flow at Rayleigh numbers closer to Ra_c than without rotation. Another important change because of rotation is found in the boundary layers. The addition of rotation leads to boundary layers that actively influence the bulk flow (Ekman 1905; Stewartson 1957; Rogers & Lance 1960). In the limit of strong rotation, at $Ro \ll 1$, the bulk flow is expected to adhere to the so-called thermal wind balance (Gill 1982). In this limit the vertical velocity is independent of the vertical coordinate, and vertical gradients of horizontal velocity only occur when there are horizontal temperature gradients.

Rotating Rayleigh–Bénard convection is relevant for many geophysical and astrophysical flow phenomena. Oceanic deep convection occurs when, in winter, surface cooling in the Arctic and Antarctic seas may lead to long-lived vortical downward flow (Marshall & Schott 1999; Gascard *et al.* 2002). This deep ventilation is of paramount importance for the global thermohaline circulation. The interiors of the giant gaseous planets are also very convective and affected by rotation (Busse & Carrigan 1976; Busse 1994), as is the outer layer of our Sun (Miesch 2000). In the liquid-metal core of our own planet, rotating convection is believed to be the driving force behind the self-sustained dynamo action (Jones 2000).

In the last decades there have been many investigations of non-rotating turbulent convection. The recent review paper by Ahlers, Grossmann & Lohse (2009) gave a comprehensive overview. The addition of rotation obviously complicates experimental investigation. Nevertheless, there have been a number of experimental investigations concerning the onset of convection and/or the convective heat transfer as a function of rotation rate (Nakagawa & Frenzen 1955; Rossby 1969; Lucas, Pfotenhauer & Donnelly 1983; Pfotenhauer, Lucas & Donnelly 1984; Pfotenhauer, Niemela & Donnelly 1987; Zhong, Ecke & Steinberg 1993; Liu & Ecke 1997; Zhong *et al.* 2009). Flow visualizations have been carried out by Boubnov & Golitsyn (1986), Zhong, Ecke & Steinberg (1993) and Sakai (1997). A typical ordering into vertically aligned vortical tubes is observed. The first local velocity (and temperature) measurements in the flow have been reported by Boubnov & Golitsyn (1990) and Fernando, Chen & Boyer (1991). Both studies used the laborious technique of particle-streak photography. The advent of digital cameras revolutionized velocity measurements. Digital recording and image procesing with particle image velocimetry (PIV; Raffel, Willert & Kompenhans 1998) allows for higher spatial and temporal resolutions, with increased ease and speed of processing. In the studies by Vorobieff & Ecke (1998*b*, 2002) PIV is applied in rotating convection, measuring in-plane displacements (and thus velocities) within a planar cross-section of the flow domain.

In numerical simulations the addition of rotation is not as cumbersome. Yet, only few numerical investigations of rotating convection have been reported. Raasch & Etling (1991) used large-eddy simulation in a simulation of the atmospheric boundary layer. Julien *et al.* (1996*a*,*b*, 1999), Kunnen, Clercx & Geurts (2006) and Kunnen, Geurts & Clercx (2009) simulated turbulent rotating convection on a horizontally periodic domain, mimicking a horizontally unbounded fluid layer. Sprague *et al.* (2006) numerically solved an asymptotically reduced set of equations valid in the limit of strong rotation. Apart from our previous work (Kunnen, Clercx & Geurts 2008*a*), the only numerical investigations of turbulent rotating convection in a cylinder in the literature are, to our knowledge, Oresta, Stringano & Verzicco (2007), Zhong *et al.* (2009) and Stevens *et al.* (2009). The first paper (Oresta *et al.* 2007) actually focuses on non-turbulent convection, but it also contains the heat transfer as a function of rotation rate at one Rayleigh number for which the fluid motion is turbulent. Zhong *et al.* (2009) compared heat transfer measurements with results from simulations, focusing on the enhancement of the heat flux under rotation and the role of the Prandtl number on this effect. Stevens *et al.* (2009) reported experimental and numerical results on transitions between turbulent states caused by the rotation.

As previously mentioned, flow visualizations by Boubnov & Golitsyn (1986), Zhong, Ecke & Steinberg (1993) and Sakai (1997) have shown that in rotating convection there is an organization into vertically aligned tube-like vortices which account for most of the vertical transport. However, it is also well known that in the absence of rotation the dominant flow feature is the so-called large-scale circulation (LSC; see Krishnamurti & Howard 1981; Brown & Ahlers 2006; Xi, Zhou & Xia 2006 and the references therein), a domain-filling circulation cell which is formed as hot plumes gather on one side of the domain and rise while the cold plumes sink on the opposite side. Inspired by Hart, Kittelman & Ohlsen (2002) and Brown & Ahlers (2006), in Kunnen *et al.* (2008*a*) we considered the effects of rotation on the LSC both experimentally and numerically. It was found that for $Ro \gtrsim 2.5$ the LSC remained the dominant flow feature; the rotation merely caused the LSC to describe a relative precession against the rotation direction of the cylinder. For $1.2 \lesssim Ro \lesssim 2.5$ a transitional region was found in which the LSC was still present but was not as strong as at higher Ro. Finally, for $Ro \lesssim 1.2$ the LSC was absent; instead, the vortical plumes were the dominant structures in the flow.

The scarcity of both experimental and numerical data concerning velocity and temperature statistics in turbulent rotating convection has prompted us to perform a combined numerical-experimental investigation of this highly relevant flow problem, with the focus on the turbulent flow statistics. The domain under study is an upright cylinder with aspect ratio $\Gamma = 1$. We limit our attention to this geometry, as it already is the default choice for experiments and numerical simulations of non-rotating convection, providing ample opportunities for comparison. Furthermore, a domain with square corners may possess unwanted corner-flow anomalies when rotation is applied. In the experiments we apply stereoscopic PIV (SPIV), a technique which records in time the three components of velocity simultaneously on many positions in a planar cross-section of the flow. The numerical part consists of direct numerical simulations (DNSs), which explicitly resolve all scales in the flow.

The remainder of this paper is as follows. In § 2 we present the experimental set-up, the measurement technique (SPIV) and the measurement procedure. The DNS method that we employ is explained in § 3, including the gathering of statistics and a validation of the resolution. The results are split into several topics. First, in § 4 we consider the turbulence intensities and their dependence on the Rossby number. Then, § 5 contains probability density functions (p.d.f.s) of the individual velocity components, vertical vorticity and temperature. The effects of various rotation rates on these distributions are examined. Next, we discuss the rotational influences on the thickness of the various boundary layers near the bottom and top plates, as well as at the sidewall, in § 6. Additionally, the mean bulk temperature gradient of rotating convection is considered. We finish the presentation of the results by comparing our previously presented experimental results on turbulence anisotropy (Kunnen, Clercx & Geurts 2008*b*) with the current numerical data on this topic (§ 7). Conclusions are drawn in § 8.

2. Experimental set-up

2.1. *Convection cell*

The convection cell and peripheral equipment are the same as used in our previous works (Kunnen *et al.* 2008*a*, *b*, *c*). A sketch of the convection cell is shown in figure 1. Letters enclosed within brackets in this section and the next refer to the labels in this sketch.

The cylindrical measurement volume of the convection cell is confined from the side with a Plexiglas tube of thickness 5 mm and inner diameter 230 mm (A). This cylinder is slid over a copper disk 30 mm thick (B) that closes the cylinder from below. Two O-ring seals are wrapped around the copper disk, making a tight fit with the cylinder.

Clamped under the copper disk is an electric resistance heater (C). At the centre of the disk a thermistor (D) is placed in a hole from below, so that the temperature

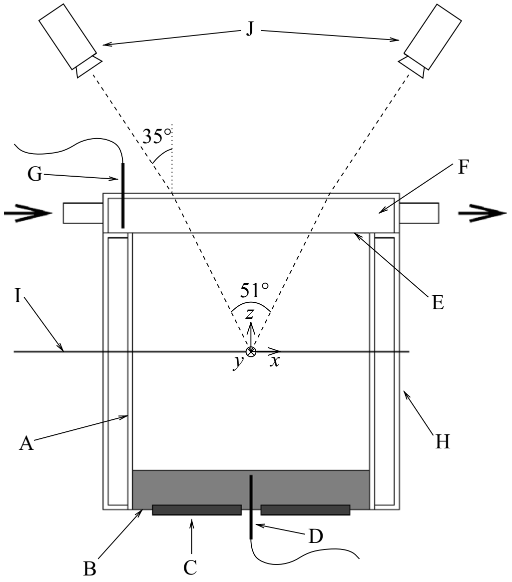

Figure 1. Sketch of the convection cell. Labels are explained in the text.

very close to the interface can be measured. This temperature probe is connected to a custom-made heater controller unit that keeps the temperature of the bottom plate at a preset value. A uniform temperature condition is maintained by the excellent heat conduction of copper. During operation, temperature fluctuations measured with the thermistor do not exceed 0.02 K. A single temperature measurement on the bottom plate does not ensure temperature uniformity across the plate. However, the effect of any temperature gradient inside the plate on the flow velocity is expected to be small, certainly when compared with the error in the SPIV measurement.

The cooling of the fluid at the top of the cylinder is complicated by the need for optical accessibility from above. At a height $H = 230\,\text{mm}$ above the copper plate the cylinder is closed with a thin sheet of Plexiglas 1 mm thick (E). (In other works, e.g. Vorobieff & Ecke 2002 and Xi *et al.* 2006, sapphire windows are employed to seal the cell from above. Sapphire has better heat conduction properties than Plexiglas. However, given the size of the current set-up, using sapphire would prove very costly. This, in addition to the ease with which Plexiglas can be used in the assembly, led us to choose a thin Plexiglas sheet.) A transparent cooling chamber (F) is placed on top. The tubes connected there are used for circulation of cooling water from a cooling bath (Haake V26/B refrigerated bath, with Haake DC50 temperature control unit). To avoid large-scale flow structuring in the flat geometry of the cooling chamber the inflow nozzles are fitted with finely meshed grids. A temperature probe (G) is placed inside the chamber, connected to the temperature controller in the cooling bath. This arrangement controls the temperature at the upper side of the cylinder. Temperature fluctuations are smaller than 0.05 K. Homogeneity of the temperature inside the cooling chamber was checked by repeatedly measuring the temperature at nine different positions inside the chamber. No mean horizontal temperature gradients were detected within the cooling chamber. At a cooling water flow rate of about $1\,\text{L}\,\text{s}^{-1}$ and a heat transfer (estimated using the Nusselt number) of approximately 40 W the horizontal temperature difference is estimated to be just under 0.01 K.

Around the cylinder is a rectangular box of Plexiglas (H). The space between the cylinder and the box is also filled with water to avoid excessive refraction on the curved cylinder surface (the refractive index of Plexiglas, $n = 1.491$, matches well with that of water, $n = 1.333$). Thus optical access from the sides is also possible.

The convection cell, and all other equipment mentioned here, are placed on a rotating table. The cylinder axis coincides with the axis of rotation. Under full load the table surface is levelled with a maximal deviation of 10 µrad. The specifications and further details of the rotating table can be found in van Bokhoven (2007).

2.2. *Measuring arrangement*

For the measurement the water is seeded with polyamid seeding particles of diameter $d = 50\,\mu\text{m}$ (Dantec Dynamics A/S). Their density $\rho = 1.03\,\text{kg}\,\text{m}^{-3}$ matches well with that of the water, $\rho = 0.997 \times 10^3\,\text{kg}\,\text{m}^{-3}$, at the mean working temperature $T = 24^\circ\text{C}$. The particles are nearly neutrally buoyant. From Lide (2007–2008), the values of the other fluid properties at this mean temperature are as follows: kinematic viscosity $\nu = 9.23 \times 10^{-7}\,\text{m}^2\,\text{s}^{-1}$, thermal diffusivity $\kappa = 1.45 \times 10^{-7}\,\text{m}^2\,\text{s}^{-1}$ and thermal expansion coefficient $\alpha = 2.50 \times 10^{-4}\,\text{K}^{-1}$. Hence the Prandtl number is $\sigma = 6.37$. These values will be used throughout the current paper. According to Raffel *et al.* (1998), the typical particle response time τ_p of such a particle to changes in the fluid flow is $\tau_p \equiv d^2\rho_p/(18\nu\rho_f)$, where ρ_p is the density of the particles and ρ_f the density of the fluid. Here $\tau_p = 1.6 \times 10^{-4}\,\text{s}$. This time should be compared with the smallest time scale that occurs in the flow. The Kolmogorov time $\tau_\eta \equiv \sqrt{\nu/\epsilon}$ is a good representation of this time scale (ϵ is the dissipation rate of turbulent kinetic energy). Using the *a priori* (non-rotating) estimate $\epsilon = \nu^3(Nu - 1)Ra/(\sigma^2 H^4)$ (Shraiman & Siggia 1990; Siggia 1994) and the Nusselt number result from Kunnen *et al.* (2008*c*), $Nu \approx 70$, we arrive at $\tau_\eta \approx 1.3\,\text{s}$. The ratio of these time scales, commonly designated the Stokes number St, is then $St \equiv \tau_p/\tau_\eta \approx 1.2 \times 10^{-4}$. The particles are responding very rapidly to changes in the flow, since $St \ll 1$. Thus we expect the particles to have velocities representative of the local fluid velocity at their respective positions.

Illumination is done with an Nd:YAG laser (Quantel CFR400, wavelength 532 nm). Using a cylindrical lens the beam is expanded to a sheet of thickness approximately 2 mm, which traverses the convection cell horizontally (I). Two vertical positions have been used: $z = 0.5H$ at mid-height and $z = 0.8H$ near the top plate. The laser is operated at 15 Hz. Above the cell two identical digital CCD cameras (J) (Megaplus ES1.0, Kodak/Roper Scientific) are mounted at off-cylinder-axis positions. Each camera points inward at an angle of 35° with the axis. Owing to the water–Plexiglas–air refractions the effective angles inside the water are 25.5°; this is the so-called stereoscopic angle (Raffel *et al.* 1998). The cameras record images with a resolution of 1008 × 1019 pixels and a 10-bit dynamic range of greyscales. Laser and camera triggering and synchronization is done with a delay generator (DG535, Stanford Research Systems). The laser and the cameras are also placed on the rotating table, to assure constant alignment.

SPIV is an extension of the regular PIV. By using two cameras instead of one it is possible to resolve the out-of-plane velocity component in addition to the in-plane components. The camera arrangement used in this work is the so-called angular displacement configuration (Raffel *et al.* 1998; Prasad 2000): the cameras are placed in such a way that their optical axes are not parallel but prescribe a so-called stereoscopic angle. This configuration generally provides the best accuracy for the out-of-plane displacements (Prasad 2000). The consequence of this configuration is that since the image and lens planes are not parallel, the object plane must also be rotated relative to the lens plane using Scheimpflug adapters. When the Scheimpflug condition (image, lens and object planes must intersect in a common line) is met the entire image is in focus. Details on the current SPIV algorithm can be found in van Bokhoven (2007). The calibration procedure is discussed in Kunnen (2008).

The measured velocity fields at $z = 0.5H$ are comprised of 49×57 vectors, with spacings $\Delta x = 1.66$ mm and $\Delta y = 1.93$ mm, for a total measurement area of approximately $9 \times 12\,\mathrm{cm}^2$. At $z = 0.8H$ the velocity fields consist of 53×55 vectors, with spacings $\Delta x = 2.30$ mm and $\Delta y = 2.78$ mm. The measurement area is roughly $12 \times 15\,\mathrm{cm}^2$ in size.

The result of the SPIV procedure is a time sequence of gridded three-component velocity data. In-plane derivatives of velocity are then easily computed using standard finite-difference formulations. In this work the vertical component of vorticity $\omega_z = (\nabla \times \boldsymbol{u})_z$ plays an important role. This quantity is determined with the contour integral formulation described by (Raffel *et al.* 1998, p. 162). Out-of-plane derivatives cannot be calculated from SPIV data. It must also be noted that SPIV, just as the regular PIV technique, smoothes and locally averages the true particle displacements: any curvature in the particle paths is linearly approximated per time step. These displacements, and hence the velocities, thus tend to be somewhat underestimated. This effect is magnified in the discrete derivatives to obtain derived quantities such as vorticity.

2.3. *Measurement procedure*

In all experiments the average temperature of the water was kept at 24°C. The gravitational acceleration is $g = 9.81\ \mathrm{m\,s^{-2}}$. The temperature difference was set to $\Delta T = 5.00$ K, which is equivalent to $Ra = 1.11 \times 10^9$. The true temperature difference over the fluid is reduced by the temperature drop over the Plexiglas top plate. A one-dimensional heat conduction analysis, using our previous Nusselt number results (Kunnen *et al.* 2008*c*) to define an effective conductivity for the convecting water layer, results in an effective Rayleigh number $Ra_{eff} \approx 6 \times 10^8$.

When the experimental temperature conditions are set the system is allowed to adapt. Once the flow has adapted to the temperature setting, the rotation is introduced. The settling time for impulsive spin-up is the so-called Ekman time scale $\tau_E \equiv H/\sqrt{\nu\Omega}$ (see e.g. van de Konijnenberg *et al.* 1994 and the references therein. At the lowest rotation rate used in this paper, $\Omega = 0.04\,\mathrm{rad\,s^{-1}}$, this time scale is $\tau_E = 1.2 \times 10^3$ s. For full adaptation a period of a few times this τ_E would be required. However, the presence of fluid motion (the LSC, as discussed in Kunnen *et al.* 2008*a*) accelerates the adaptation to the rotation compared with a still fluid. From the model of the LSC under rotation presented in Kunnen *et al.* (2008*a*), we estimate an ‘LSC settling time’ $\tau_s \approx 7 \times 10^2$ s. Therefore, for the lowest rotation rates the system is allowed to adapt for at least half an hour. Vorobieff & Ecke (1998*a*) showed in their spin-up experiments of convection that indeed the transition takes only a fraction of τ_E at lower rotation rates. At the larger $\Omega \gtrsim 0.1\,\mathrm{rad\,s^{-1}}$ this time can be lessened, as then $\tau_E < \tau_s$ and the faster Ekman dynamics govern the adaptation.

The settings for the SPIV measurement series at both heights are presented in table 1, with the corresponding values of the dimensionless numbers Ta and Ro as defined in (1.1) and (1.2). In each of these experiments 10^4 velocity maps have been obtained at a rate of 15 Hz, a duration of just over 11 min per measurement.

Centrifugal forces may become important at high rotation rates. A convenient ratio to quantify the relative importance of the centrifugal acceleration to the gravitational acceleration is the Froude number $Fr \equiv \Omega^2 D/(2g)$ (Hart 2000). In the

Ω (rad s^{-1})	*Ta*	*Ro*
0	0	∞
0.04	2.10×10^{7}	2.89
0.08	8.41×10^{7}	1.44
0.16	3.36×10^{8}	0.721
0.32	1.35×10^{9}	0.361
0.64	5.38×10^{9}	0.180
1.28	2.15×10^{10}	0.090

Table 1. Parameters for the measurement series.

current experiments, at the highest rotation rate $\Omega = 1.28$ rad s^{-1}, the Froude number is still quite small, i.e. $Fr \approx 0.02$. Centrifugal effects will hence be neglected.

3. Numerical arrangement

3.1. *Problem description, numerical procedure and statistics*

The equations of motion that govern the flow are the Navier–Stokes and heat equations, with the constraint of incompressibility. Within the Boussinesq approximation (Chandrasekhar 1961), these equations are

$$\left.\begin{aligned} \frac{\partial \boldsymbol{u}}{\partial t} + (\boldsymbol{u}\cdot\nabla)\boldsymbol{u} + \frac{1}{Ro}\hat{z}\times\boldsymbol{u} &= -\nabla p + T\hat{z} + \sqrt{\frac{\sigma}{Ra}}\nabla^2\boldsymbol{u}, \\ \frac{\partial T}{\partial t} + (\boldsymbol{u}\cdot\nabla)T &= \frac{1}{\sqrt{\sigma Ra}}\nabla^2 T, \\ \nabla\cdot\boldsymbol{u} &= 0. \end{aligned}\right\} \tag{3.1}$$

Here $\boldsymbol{u}$ is the velocity vector; t stands for time; $\hat{z}$ is the unit vector pointing upward; p is the reduced pressure; and T represents the temperature. The equations have been non-dimensionalized as follows. Velocity is scaled with the so-called free-fall velocity $U \equiv \sqrt{g\alpha\Delta T H}$ (Prandtl 1932). Lengths are scaled with the separation H of the bottom and top plates. Temperatures are converted according to $T = (T^* - T_0)/\Delta T$, where T^* is the actual temperature and T_0 the temperature of the upper plate.

Because of the current cylindrical geometry, it is advantageous to formulate the problem in cylindrical coordinates (r, ϕ, z) which indicate the radial, azimuthal and vertical components, respectively. The corresponding velocity vector is (u_r, u_ϕ, u_z). No-slip velocity boundary conditions are applied at all walls. Temperatures are constant at the bottom and top plates: $T = 1$ at $z = 0$ and $T = 0$ at $z = H$. The sidewall is thermally insulating: $\partial T/\partial r = 0$ at $r = H/2$.

In cylindrical coordinates the governing equations (3.1) possess terms that include a factor $1/r$. These need special treatment to be evaluated at the cylinder axis $r = 0$ (Verzicco & Orlandi 1996). The equations are discretized on the staggered grid by central finite-difference formulations of second-order accuracy. The solution uses a fractional-step procedure with the elliptic equation inverted using trigonometric expansions in the azimuthal direction and a direct solver for the other two directions. Details can be found in Verzicco & Orlandi (1996) and Verzicco & Camussi (1997, 1999, 2003).

The gathering of statistical data is carried out in two ways. First, averaging in the azimuthal direction of the three velocity components, temperature and pressure is carried out, as well as calculation of their root-mean-square (r.m.s.) values. Also, the dissipation rate of kinetic energy $\epsilon \equiv \sqrt{\sigma/Ra}|\nabla \boldsymbol{u}|^2$ and the thermal variance dissipation rate $N \equiv |\nabla T|^2/\sqrt{\sigma Ra}$ are calculated and averaged in the azimuthal direction. Second, numerical probes positioned at several grid cells record time histories of the three components of velocity $\boldsymbol{u}$ and vorticity $\boldsymbol{\omega} \equiv \nabla \times \boldsymbol{u}$, temperature and pressure. Two series of 150 numerical probes each are placed at respective heights $z = 0.5H$ and $z = 0.8H$, stretching from $r = 0.25H$, $\phi = 0$, through $r = 0$, to $r = 0.25H$, $\phi = \pi$ in straight lines.

3.2. *Parameters and resolution*

In all simulations we set $Ra = 1 \times 10^9$ and $\sigma = 6.4$. This corresponds with our experiments on turbulent convection in water. We take this Rayleigh number rather than Ra_{eff}, since the latter is not known within reasonable accuracy; furthermore, such modest differences in Ra are not expected to cause significant qualitative differences in the results. The Rossby numbers that are used in the simulations cover nearly three decades: $Ro = 0.045$, 0.068, 0.090, 0.18, 0.36, 0.72, 1.08, 1.44, 1.80, 2.16, 2.52, 2.88, 5.76 and 11.52.

The number of grid points in the radial, azimuthal and verticals direction are $N_r \times N_\phi \times N_z = 193 \times 385 \times 385$. The distribution of grid points in the radial and vertical directions was not uniform: close to the walls a denser grid is applied than in the centre. For validation of this resolution we follow the criteria of Verzicco & Camussi (2003). These authors have made a distinction between boundary-layer and bulk resolution. In the bulk flow the smallest length scales to be resolved are the Kolmogorov length η and the Batchelor length η_T. In the current dimensionless variables these are

$$\eta = \left(\frac{\sigma}{Ra}\right)^{3/8} \epsilon^{-1/4}, \quad \eta_T = \eta\, \sigma^{-1/2}. \tag{3.2}$$

Since $\sigma > 1$ the smallest of these is the Batchelor length (i.e. temperature structures are finer than velocity structures in the flow). In the bulk the grid spacing should not be too large compared with η_T (a maximal grid spacing of $4\eta_T$ was found to be acceptable in Kerr & Herring 2000 and Verzicco & Camussi 2003). An inventory of local dissipation ϵ at the centre of the domain and at the various Ro values was carried out. It was found that ϵ generally increases there when rotation is added and that ϵ at the centre of the domain is maximal at $Ro = 0.18$. At that Ro the smallest bulk lengths $\eta \approx 8 \times 10^{-3}$ and $\eta_T \approx 3 \times 10^{-3}$ are found. The maximal grid spacing is $\Delta z = 0.0048$. Hence the bulk resolution is sufficient according to Verzicco & Camussi (2003).

The near-wall resolution is mainly determined by the thickness of the thermal and viscous boundary layers, as enough grid points should be found within these layers. Verzicco & Camussi (2003) put forward the criterion that at least six points should be found within the thinnest of the thermal and viscous boundary layer. As $\sigma > 1$ the thermal boundary layer is expected to be thinner than the viscous layer. However, it is expected that under rotation the viscous boundary layer is considerably thinner (cf. the Ekman boundary layer; see e.g. Gill 1982; Pedlosky 1987). The very thin Ekman boundary layers under strong rotation indeed posed considerable constraints in terms of near-wall resolution. In an *a posteriori* check, at $Ro = 0.045$ (for which the thinnest boundary layers are found; see figure 14) there were only 10 grid points found within the viscous boundary layer, which had decreased in size past the thermal boundary layer. Still, the near-wall resolution is well within the specified criterion and is considered adequate.

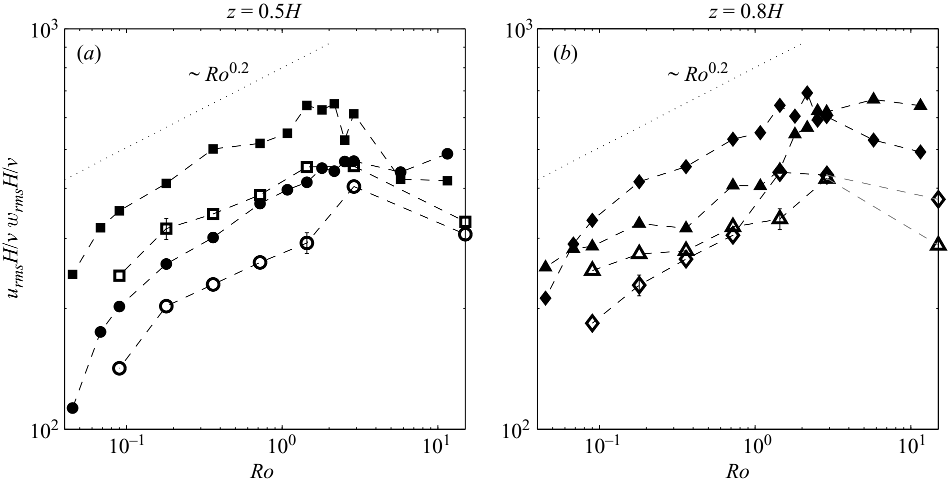

FIGURE 2. Normalized r.m.s. velocities and their variation with Ro. (a) At $z = 0.5H$ the horizontal r.m.s. values u_{rms} are indicated with circles and the vertical r.m.s. values w_{rms} with squares. (b) At $z = 0.8H$ the horizontal components u_{rms} are plotted with triangles and the vertical r.m.s. values w_{rms} with diamonds. The filled symbols are simulation results, while the open symbols are from the experiments. The symbols on the right-hand-side boundary of both figures are at $Ro = \infty$. For reference, a power-law dependence $Ro^{0.2}$ is included with the dotted line. Representative error bars for the experimental results are also included.

A third validation that is applied in Verzicco & Camussi (2003) concerns the Nusselt number results. The Nusselt definition based on the mean temperature gradient at the plates is sensitive to the near-wall resolution used. The other definition based on the volume-and-time average of conductive and convective fluxes is more sensitive to the bulk resolution. The results from both definitions were found to match within 1 % in all of the considered cases, reinforcing that both bulk and boundary-layer resolution is appropriate for simulations in the current parameter range.

4. Turbulence intensities

Since the critical Rayleigh number for onset of convection goes up when a rotation is added (Chandrasekhar 1953, 1961), it is generally believed that rotation stabilizes the turbulent flow; i.e. turbulent fluctuations are diminished. The strength of the turbulent fluctuations is represented here with the r.m.s. values of velocity, vertical vorticity and temperature. In figure 2 the horizontal and vertical r.m.s. velocities are plotted as a function of Ro. The values are taken at two vertical positions, namely $z = 0.5H$ and $z = 0.8H$. The experimentally obtained values are normalized by ν/H, which requires the numerical results to be multiplied by a factor $\sqrt{Ra/\sigma}$. For the simulations, the horizontal r.m.s. velocity u_{rms} is taken as the r.m.s. value of the azimuthal velocity u_ϕ, as calculation of u_r near the axis is difficult (Verzicco & Orlandi 1996).

Similarly, we also report the r.m.s. values of the vertical vorticity ω_{rms} in figure 3, where the experimental data are normalized by ν/H^2 and the numerical data are multiplied by $\sqrt{Ra/\sigma}$ for compliance. The effects of rotation can be roughly divided into two regimes: one for $Ro \gtrsim 1$, where the presence of the LSC is characteristic (Kunnen *et al.* 2008*a*), and one for $Ro \lesssim 1$, for which the vortical columns are dominant.

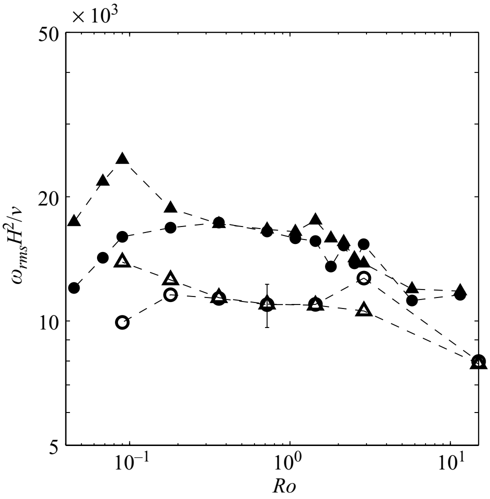

FIGURE 3. The r.m.s. values of vertical vorticity ω_{rms} as a function of Ro. The circles denote $z = 0.5H$, while the triangles are for $z = 0.8H$. The filled symbols are taken from the simulations, while the open symbols are from the experiments. The symbols on the right-hand-side axis are at $Ro = \infty$; a representative error bar for the experimental data is included.

For the regime $Ro \gtrsim 1$ it is found that velocity fluctuations increase compared with the corresponding values at $Ro = \infty$. It is plausible that the LSC, with its added azimuthal drift dynamics (Kunnen *et al.* 2008*a*), is responsible for the increased horizontal fluctuations. Concerning the vertical-velocity fluctuations, we also wish to mention the boundary-layer effect known as Ekman pumping (Ekman 1905; Gill 1982; Pedlosky 1987). Under rotation the viscous (Ekman-like) boundary layers respond to the presence of vertical vorticity by enacting a vertical motion directed towards (away from) the plate in case of anticyclonic (cyclonic) vorticity. The increased vorticity fluctuations as Ro crosses 3 (see figure 3) coinciding with a similar increase of w_{rms} around the same Ro value may be an indication that Ekman pumping becomes active around $Ro \approx 3$.

At $Ro \lesssim 1$ both horizontal and vertical velocity fluctuations are decreasing with decreasing Ro. For reference, a power-law relation $Ro^{0.2}$ is included in figure 2(*a*, *b*). In this regime the rotation attenuates the vertical turbulence intensities. As the horizontal fluctuations are directly related to the vertical fluctuations (the forcing of the flow is in the vertical direction) these follow the same trend. The leftmost points, at $Ro \lesssim 0.1$, show a different scaling regime with stronger rotational dependence, where the fluctuations are strongly damped as the stable non-convective situation is approached in which convection is fully suppressed by rotation. For a horizontally unbounded fluid layer, Chandrasekhar (1961) showed that the critical Rayleigh number Ra_c for onset of convection is dependent on Ta: $Ra_c = 8.7\,Ta^{2/3}$, which leads to $Ro_c = 0.011$ in this case (Ro_c is the critical Rossby number; for $Ro < Ro_c$ at constant Ra and σ convection is suppressed by rotation). However, for a cylindrical geometry Goldstein *et al.* (1993) and Zhong *et al.* (1993) reported a smaller Ro_c. Extrapolating their results to the current Rayleigh number gives an approximate value $Ro_c \simeq 1 \times 10^{-4}$, much smaller than $Ro = 0.045$, which is the lowest value of Ro considered here.

There is a difference in the behaviour at the two measurement heights. The horizontal velocity fluctuations at $z=0.8H$ (triangles in figure 2*b*) have a flatter slope for $Ro \lesssim 0.3$ than the other curves. The near-plate dynamics of the vortical columns are reflected here, namely the convergent flows feeding the vortex columns and the divergent flows that occur as the fluid has reached the vertically opposite side of the domain. Another remarkable finding concerns the fluctuations at $z=0.5H$. It is found that the rotation induces considerable anisotropy, in the sense that vertical fluctuations are considerably larger than horizontal fluctuations. For a further discussion, see § 7.

The effects of rotation on the velocity fluctuations are remarkably different from non-convective rotating turbulence (van Bokhoven *et al.*, submitted), where it is found that the rotation suppresses the vertical fluctuations and that horizontal velocities are larger. In the current work it is found that in rotating convection vertical fluctuations are larger than horizontal fluctuations at all rotation rates. The major difference is that in convection the convective forcing is directed vertically, while in van Bokhoven *et al.* (submitted) forcing is applied in all three directions. In the current work, only at $z=0.8H$ and for the lowest Rossby numbers, the horizontal fluctuations are larger than in the vertical direction. This is here expected to be caused by the proximity of the plate and the spin-up and spin-down of vortical plumes taking place there, which is accompanied by strong horizontal motions.

The experimental results for both horizontal and vertical r.m.s. velocities at the two measurement heights show excellent qualitative agreement with those of the simulations. Quantitatively, the experimental velocity r.m.s. values are approximately 25 % below the numerical results. Losses because of the non-perfect boundary conditions of the experiment as compared with the 'ideal' boundaries in the simulations lead to a reduced effective Rayleigh number and reduced turbulence intensities in the experiment. Furthermore, the aforementioned underestimation of particle displacements by SPIV may enhance the discrepancy. The results of preliminary simulations at $Ra=6\times10^8$ (not included in this paper) indeed show a better quantitative agreement with the experimental data.

The vorticity fluctuations in a range of Rossby numbers around $Ro=1$ remain rather constant. At the lowest Ro values considered here, however, different trends are noticed for ω_{rms} at the two heights under consideration. At mid-height ($z=0.5H$) ω_{rms} shows a mild decrease with decreasing Ro while increasing near the top plate ($z=0.8H$). The injection of vorticity close to the plates can thus be directly detected here. Rotation enhances the kinetic energy dissipation ϵ in the centre, peaking at $Ro=0.18$, which is also reflected in the peak ω_{rms} value for $z=0.5H$ at that Ro. For $Ro \lesssim 0.1$, however, the damping of the convection by rotation is also observed in the ω_{rms} plots. The qualitative agreement between experiment and simulation is again very good. However, quantitatively the separation is larger than in the velocity r.m.s. values. This is again due to the lower effective Rayleigh number in the experiment. Additionally, the numerical evaluation of vorticity is more accurate in the DNS because of its higher spatial resolution. Local gradients are better resolved. Nevertheless, an encouraging agreement between simulation and experiment is found.

The current results for velocity and vorticity fluctuations can be compared to those of Vorobieff & Ecke (2002), who used a water-filled cell of aspect ratio $\Gamma=1$. Although different Rayleigh and Prandtl numbers were used in their work (Vorobieff and Ecke applied $Ra=3.2\times10^8$ and $\sigma=5.81$), the observed trends should be similar. In that study the horizontal velocity fluctuations were measured using PIV. The horizontal fluctuations at $z=0.5H$ were reported to slowly decrease with decreasing Ro. Measurements in the plane directly below the upper plate revealed that there the

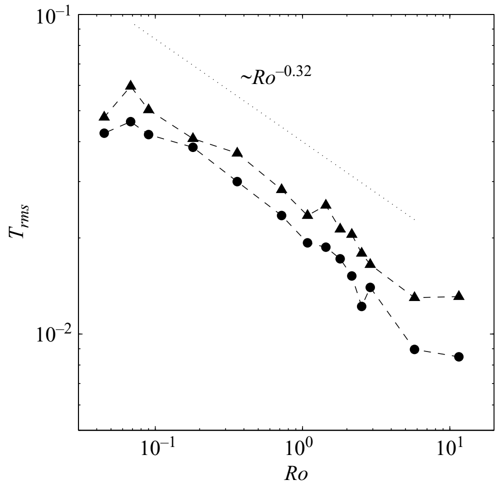

FIGURE 4. The r.m.s. values of temperature T_{rms} as a function of Ro. Circles are values at $z = 0.5H$, while the triangles are for $z = 0.8H$. A reference power-law slope $Ro^{-0.32}$ is also included (dotted line).

horizontal velocity fluctuations are largely independent of rotation rate; the current results from somewhat deeper inside the cell at $z = 0.8H$ show a stronger dependence on Ro. For the vorticity fluctuations the near-wall measurements of Vorobieff & Ecke (2002) showed a dramatic increase as Ro decreases. This effect is not as large in the current study, since our 'near-wall' experiment is still quite far from the plate. As the vortices are formed very close to the plates the effect is expected to be the strongest at that vertical position. The vorticity fluctuations at mid-height showed a similar trend as in the current study. The drop-off around $Ro \approx 0.1$ found by Vorobieff & Ecke (2002) is also reproduced.

A stronger dependence on Ro is found for the r.m.s. temperatures, shown in figure 4. Experimental data for T_{rms} are unavailable, since no temperature measurements have been carried out. The r.m.s. temperatures increase when rotation is enhanced (in other words Ro decreases). Although not exactly matching, a representative power law would be $Ro^{-0.32}$, which is also included in figure 4. It is representative of the results at both $z = 0.5H$ and $z = 0.8H$. Only at the lowest value of Ro, i.e. $Ro = 0.045$, there is a small drop-off in T_{rms}. For $Ro \gtrsim 5$ there is hardly any effect of rotation on T_{rms}. Under rotation the vortical plumes that develop need considerably more thermal contrast to break out from the boundary layer into the bulk fluid, as the critical Ra has increased. The T_{rms} values at $z = 0.8H$ are consistently larger than at $z = 0.5H$. This is a sign of the formation of vortical plumes near the plate, leading to higher T_{rms} values at $z = 0.8H$.

In this section it is indeed observed that rotation stabilizes the flow, in the sense that rotation diminishes the strength of the turbulent velocity fluctuations. However, this statement is only valid for $Ro \lesssim 3$. Around this Rossby number $Ro \approx 3$ a significant step in the magnitudes of vertical-velocity and vertical-vorticity fluctuations is found, pointing at the Ekman pumping mechanism becoming active for this rotation rate (and higher). The process of stabilization by rotation is observed in the velocity fluctuations that are reduced when the Rossby number is decreased, while the temperature fluctuations grow stronger. However, owing to the Ekman pumping, the vorticity

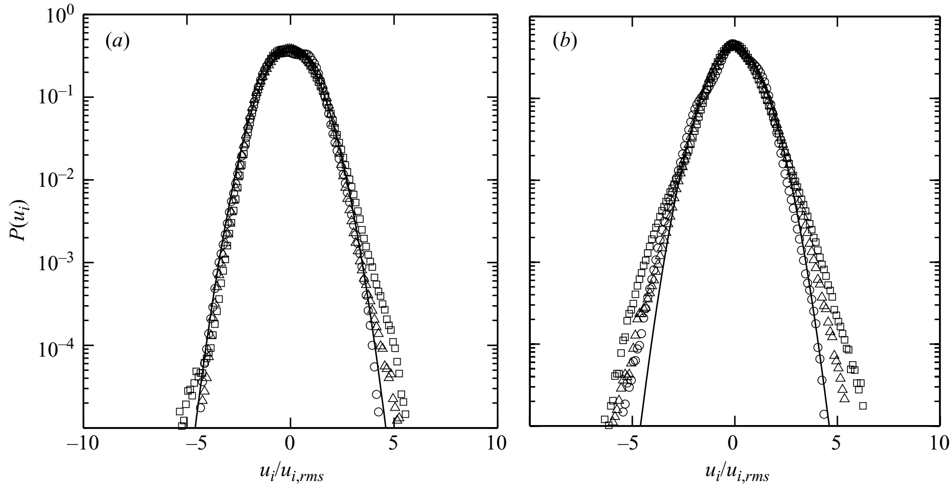

FIGURE 5. Normalized experimental p.d.f.s of velocity fluctuations u (circles), v (triangles) and w (squares) at $Ra = 1.11 \times 10^9$, $\sigma = 6.37$ and $Ro = \infty$ at heights (a) $z = 0.5H$ and (b) $z = 0.8H$. The solid lines represent reference Gaussian distributions.

fluctuations are increased with decreasing Ro, especially near the plates. Only at the lowest $Ro \lesssim 0.1$ under consideration there is a strong damping observed in all r.m.s. values considered here.

5. Probability density functions

5.1. *Velocity statistics*

The p.d.f.s of velocity in non-rotating convection are known to be Gaussian from many measurements (Ashkenazi & Steinberg 1999; Qiu & Tong 2001; Vorobieff & Ecke 2002; Qiu *et al.* 2004; Verdoold *et al.* 2008) and numerical simulations (Balachandar & Sirovich 1991; Camussi & Verzicco 2004). This is confirmed with our measurements presented in figure 5, where the p.d.f.s of the three velocity components are shown at the two measurement positions, namely $z = 0.5H$ and $z = 0.8H$. At height $z = 0.8H$ (figure 5b) the p.d.f.s are somewhat widened, especially that of the vertical velocity w. The presence of coherent structures (plumes) raises the probability of extreme events to some degree, thereby widening the p.d.f.

In figure 6 the velocity p.d.f.s at several rotation rates (Rossby numbers) obtained from the experiments are depicted. For clarity, the plots are divided over two sub-parts: each plot pair has on the left the cases $Ro \geqslant 0.72$ and the cases $Ro \leqslant 0.36$ on the right. Figure 6(a–d) shows that the distribution of horizontal fluctuations hardly changes when rotation is added; the p.d.f.s remain close to the Gaussian shape. Vorobieff & Ecke (2002) showed experimentally that under rotation the p.d.f.s of the horizontal velocity components did not change by much: they observed a development of weak exponential tails, especially close to the top plate. This development was related to the organization of the flow into small-scale vortices. The shapes of the horizontal-velocity p.d.f.s found here reproduce those of Vorobieff & Ecke (2002) well. The simulations give similar results (see figure 7a–d, which has a similar division of the plots). The distributions of horizontal velocity fluctuations (represented here with the azimuthal velocity component u_ϕ) are very similar to those found in the experiments.

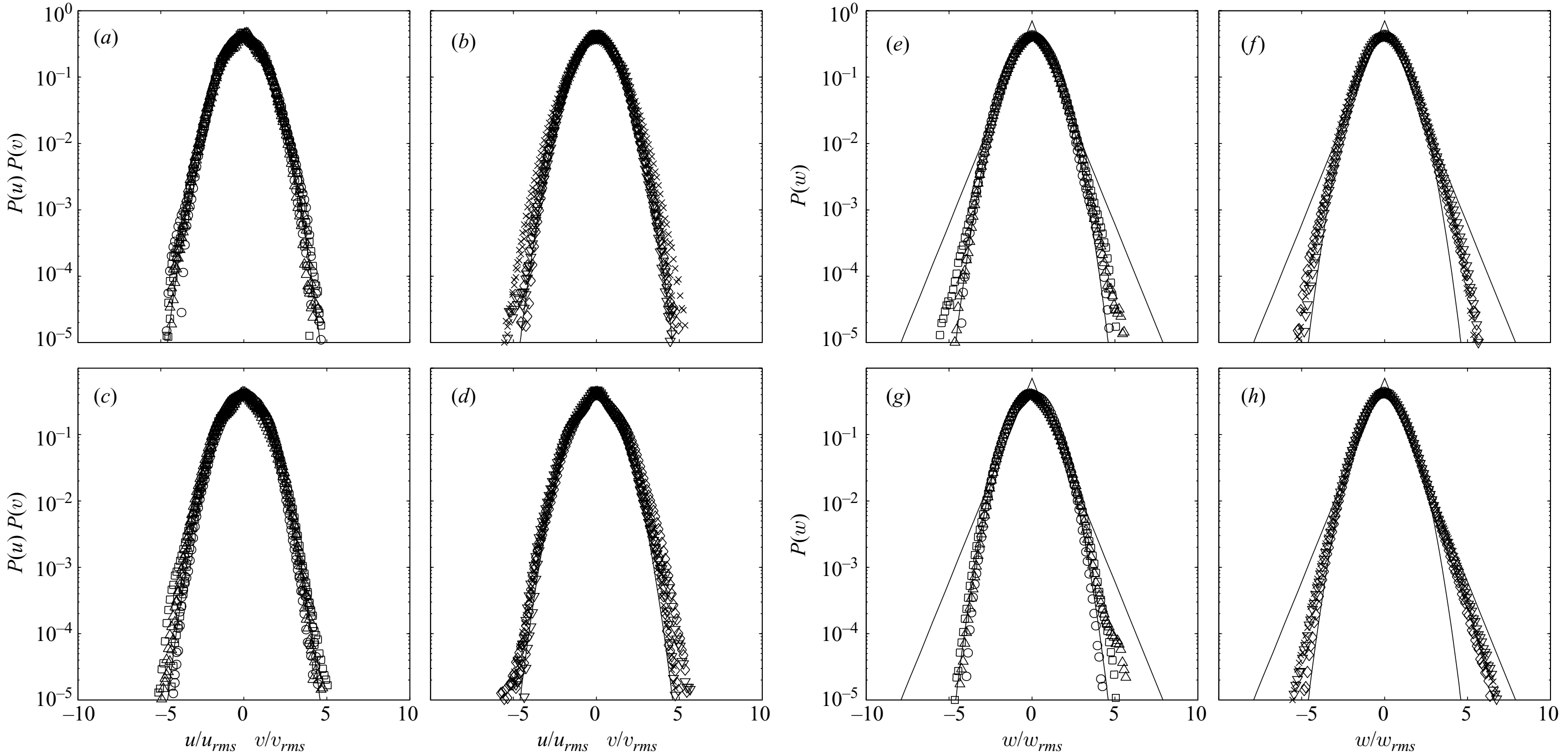

FIGURE 6. Normalized experimental p.d.f.s of horizontal velocity fluctuations u, v at (a, b) $z = 0.5H$ and (c, d) $z = 0.8H$. A reference Gaussian distribution is also included (solid line). Normalized experimental p.d.f.s of vertical velocity fluctuations w at (e, f) $z = 0.5H$ and (g, h) $z = 0.8H$. Reference Gaussian and exponential distributions are also included (solid lines). In (a, c, e, g) the Rossby numbers $Ro \geqslant 0.72$ are included: $Ro = 2.89$ (circles), 1.44 (upright triangles) and 0.72 (squares). In (b, d, f, h) the Rossby numbers $Ro \leqslant 0.36$ are shown: $Ro = 0.36$ (diamonds), 0.18 (downward-facing triangles) and 0.090 (crosses).

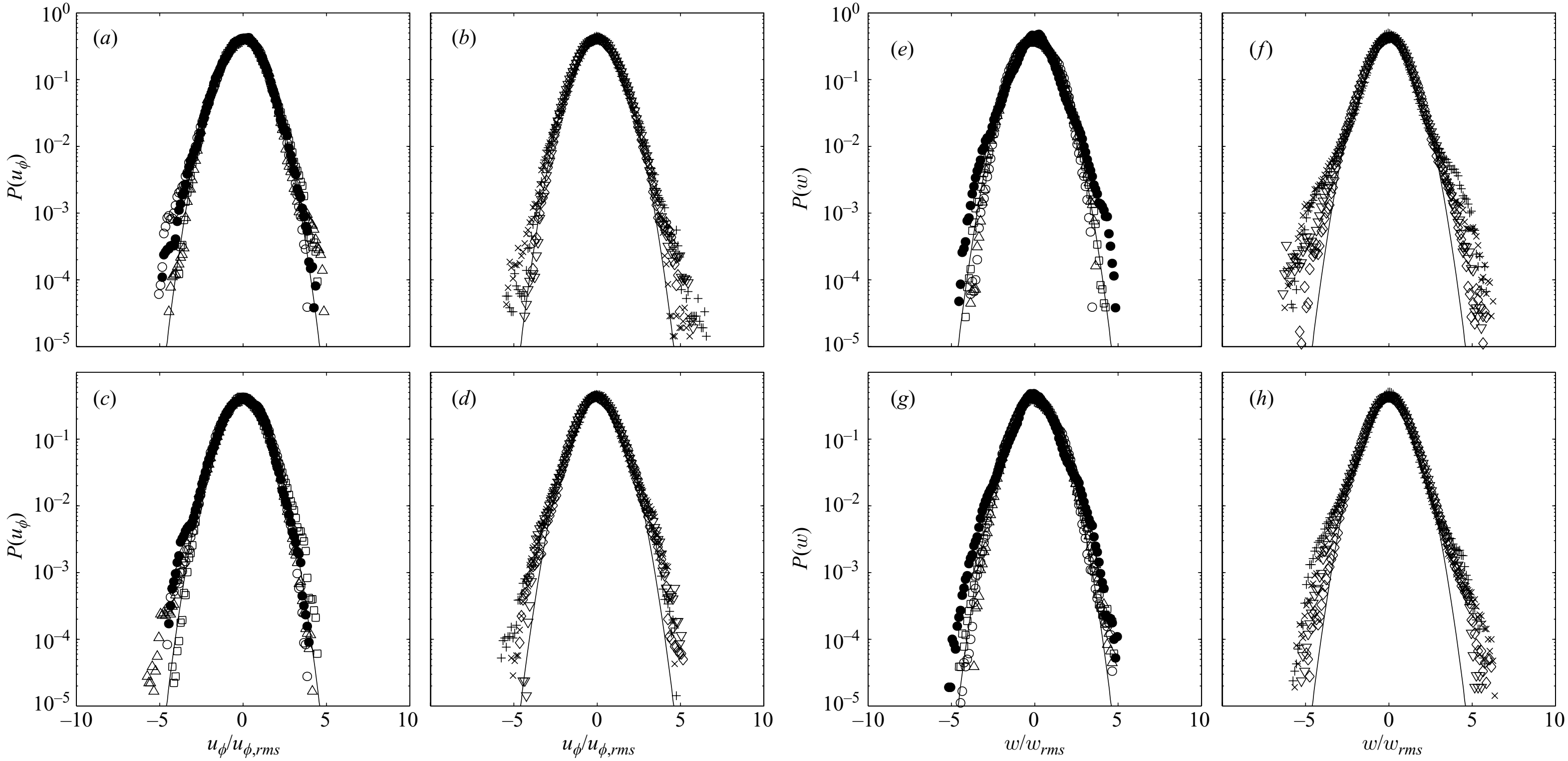

FIGURE 7. Normalized numerical p.d.f.s of horizontal velocity at (*a*, *b*) $z = 0.5H$ and (*c*, *d*) $z = 0.8H$ from the simulations; p.d.f.s of vertical velocity at (*e*, *f*) $z = 0.5H$ and (*g*, *h*) $z = 0.8H$. In (*a*, *c*, *e*, *g*) the Rossby numbers $Ro \geqslant 0.72$ are included: $Ro = 11.52$ (filled circles), 2.88 (open circles), 1.44 (upright triangles) and 0.72 (squares). In (*b*, *d*, *f*, *h*) the Rossby numbers $Ro \leqslant 0.36$ are shown: $Ro = 0.36$ (diamonds), 0.18 (downward-facing triangles), 0.090 (crosses) and 0.045 (pluses). The solid lines are reference Gaussian distributions.

The influence of rotation on the vertical velocity p.d.f. has not been reported as extensively in literature. In simulations at $Ro = 0.75$ by Julien *et al.* (1996*b*), near the boundary layer, a wider distribution was found with skewness towards motion directed away from the boundary. In simulations reported in Kunnen *et al.* (2006) we confirmed this skewness behaviour but also saw an opposite trend (skewness favouring motion towards the plate) in a vertical range starting just outside the boundary layer. In figure 7(*e*–*h*) we show the vertical-velocity p.d.f.s from the current simulations. They feature, at both considered heights, a development of wider tails, especially for the lower Ro values. No strong asymmetry is observed in the distributions. In figure 6(*e*, *f*) the experimental p.d.f. of vertical velocity at $z = 0.5H$ confirms the aforementioned behaviour. Contrarily, in figure 6(*g*, *h*) the experimental p.d.f.s of vertical velocity at $z = 0.8H$ do develop an asymmetry. The skewness

$$S \equiv \frac{\langle w^3 \rangle}{\langle w^2 \rangle^{3/2}} \tag{5.1}$$

is a dimensionless measure for the asymmetry of a p.d.f. (w can be replaced by any other variable): it is positive when the tail on the positive side is largest and negative when the negative tail is dominant. The positive skewness found here ($S \approx 0.2$ for all cases $Ro \leqslant 1.44$) indicates that extreme positive values are slightly more probable and, consequently, that (positive) upward velocity towards the top plate is spatially confined to a somewhat smaller area than downward velocity (Moeng & Rotunno 1990; Kerr 1996; Kunnen *et al.* 2006). This effect actually goes against the behaviour very close to the plate, reported by Julien *et al.* (1996*b*), that the vertical-velocity p.d.f. is skewed towards motion directed away from the boundary. In the current work there is a discrepancy between experiment and simulation concerning the skewness. A possible explanation is presented in several steps. (i) Owing to the poorer thermal conductivity of the plate in the experiments relative to the simulations, there is less buoyancy added to a plume as it is formed. (ii) The plume undergoes a smaller buoyant acceleration and also less spin-up by vortex stretching. This lessens the lateral confinement of cold plumes in the experiments. (iii) Hence, the downward velocity is not as strongly confined into strong small-scale structures; the negative/left-hand side of the p.d.f. does not show an enhanced tail.

5.2. *Vorticity statistics*

The distributions of the vertical component of vorticity in turbulent convection without rotation are known to be exponential (Balachandar & Sirovich 1991; Vorobieff & Ecke 2002; Zhou, Sun & Xia 2007). The exponential shape of the p.d.f.s is reproduced here, both in the experiments (figure 8) and in the simulations (the highest $Ro = 11.52$ is included in figure 9, where only minimal influence of rotation is present). Generally, for example in Castaing, Gagne & Hopfinger (1990), the exponential shape of the vorticity p.d.f.s is related with the stronger intermittency of velocity derivatives than of velocity itself. Physically, this points at a concentration of strong vorticity into localized structures.

The interaction of the fluid with the horizontal plates in turbulent rotating convection leads to injection of strong cyclonic (vertical) vorticity into the flow near the bottom and top plates. This effect can be observed in the p.d.f.s of vertical vorticity at various Rossby numbers. Depicted in figure 9 are the p.d.f.s obtained from the simulations; figure 10 presents the p.d.f.s from the experiments, with a similar division of the plots as before, i.e. $Ro \geqslant 0.72$ on the left-hand side and $Ro \leqslant 0.36$ on the right-hand side. When rotation is added a considerable preference for cyclonic

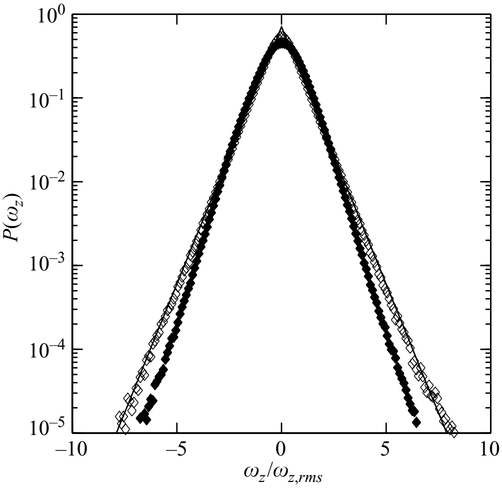

FIGURE 8. Normalized experimental p.d.f.s of the vertical vorticity component ω_z at $Ro = \infty$ (no rotation), for $z = 0.8H$ (filled symbols) and $z = 0.5H$ (open symbols). A reference exponential distributions is also included (solid line).

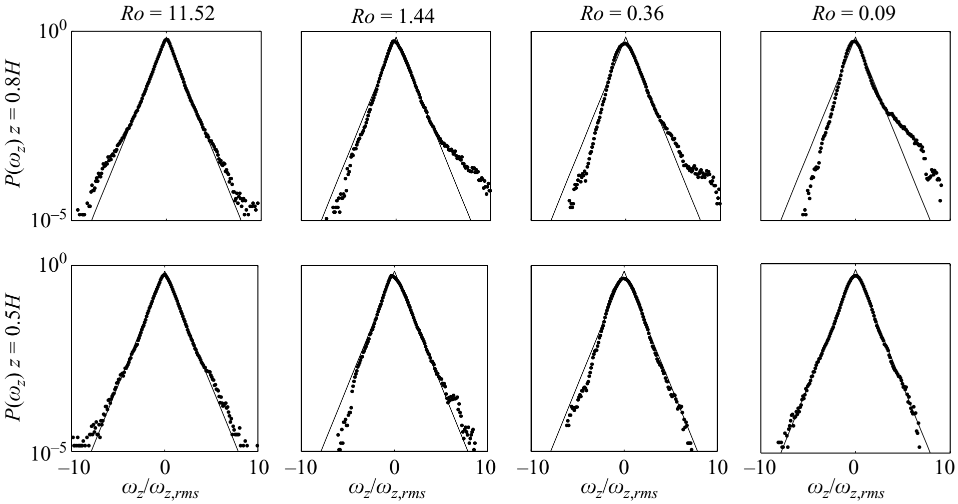

FIGURE 9. Normalized p.d.f.s of the vertical vorticity component ω_z from the simulations at selected Ro values, for $z = 0.8H$ (upper row) and $z = 0.5H$ (lower row). Reference exponential distributions are also included (solid lines).

vorticity is developed (Julien *et al.* 1996*b*; Vorobieff & Ecke 2002), as is shown by the enhancement of the right-hand-side tail relative to the left-hand-side tail. This is especially true for the off-centre position $z = 0.8H$ (upper row in figure 9 and figure 10*c*,*d*), a sign of the formation of the vortical plumes near the plates. The main difference between the results from the experiments and from the simulations is that the tails are much more pronounced in the simulation results. As noted before in §4, apart from the lower effective Rayleigh number in the experiment, the smaller experimental resolution and error propagation in the discrete derivatives tend to reduce the width of the measured vorticity distribution.

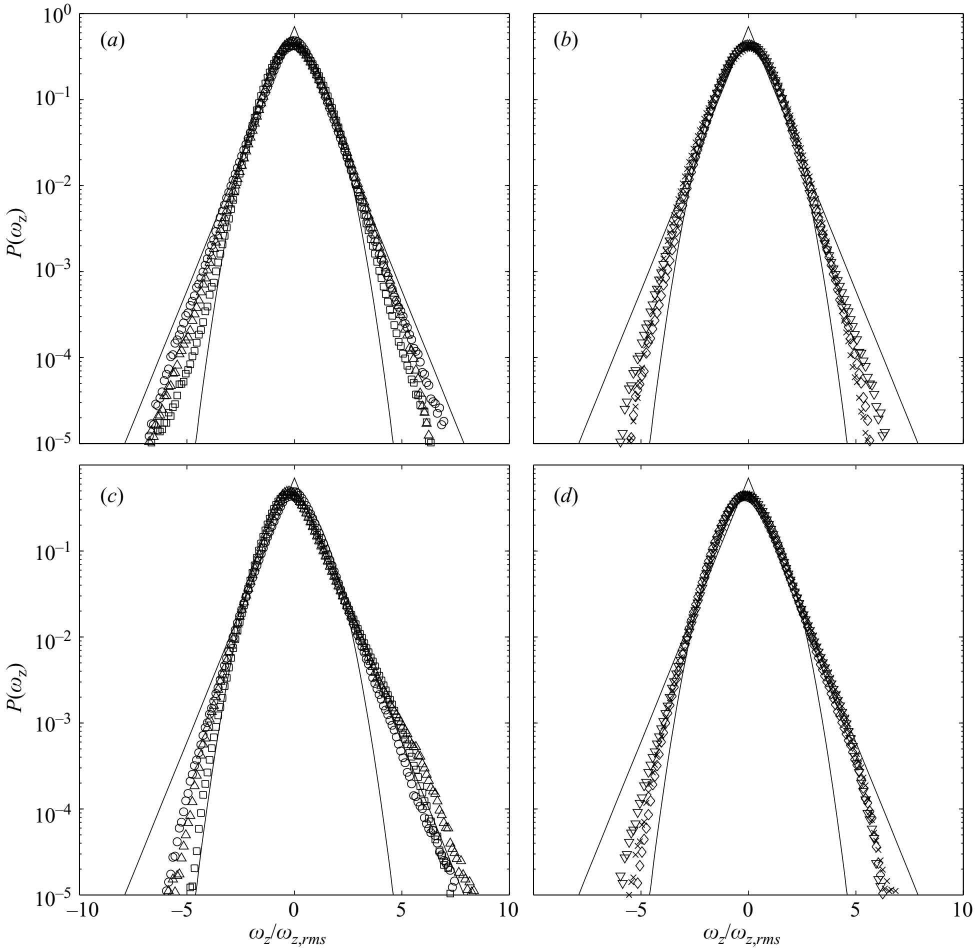

FIGURE 10. Normalized experimental p.d.f.s of vertical vorticity fluctuations ω_z at (*a*, *b*) $z = 0.5H$ and (*c*, *d*) $z = 0.8H$. Reference Gaussian and exponential distributions are also included (solid lines). In plots on the left the Rossby numbers $Ro \geqslant 0.72$ are considered: $Ro = 2.89$ (circles), 1.44 (upright triangles) and 0.72 (squares). On the right the Rossby numbers $Ro \leqslant 0.36$ are included: $Ro = 0.36$ (diamonds), 0.18 (downward-facing triangles) and 0.090 (crosses).

To quantify the asymmetry in the vorticity distributions their skewnesses S_{ω_z} have been calculated. The changes of S_{ω_z} with Ro are depicted in figure 11, for both experiments (open symbols) and simulations (filled symbols). The skewness is mostly positive, pointing at the input of positive vorticity by Ekman pumping near the plates. We first discuss the skewness at $z = 0.5H$ (squares) from experiment and simulation. They are qualitatively similar, although there is again a quantitative disagreement. We expect that this is mostly an issue of grid resolution, which is important in the calculation of discrete velocity derivatives for vorticity. The skewness around $Ro \sim 1$ is positive, while at higher and lower Ro nearly symmetric distributions are found at mid-height, $z = 0.5H$. This effect can also be found in the work of Vorobieff & Ecke (2002), although not as pronounced, since only one of their measurements is at a Rossby number of order one. Julien *et al.* (1996*b*) and Vorobieff & Ecke (2002)

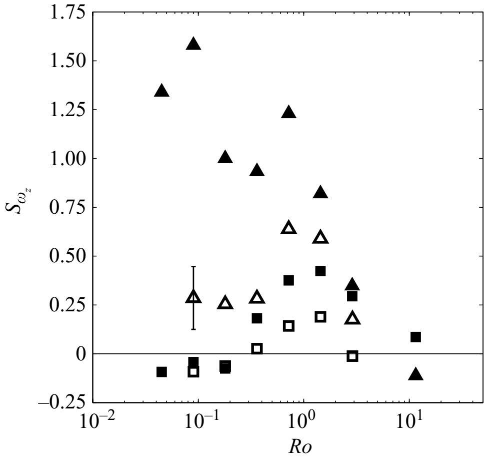

FIGURE 11. Skewness of ω_z and its dependence on Ro. The filled symbols are numerical results; the open symbols are from experiments. Squares represent S_{ω_z} calculated at $z = 0.5H$, and triangles represent S_{ω_z} calculated at $z = 0.8H$. A representative error bar for the experimental results is included.

mentioned that anticyclonic vortical structures are unstable when their vorticity is large compared with the rotation: $\omega > 2\Omega$. Indeed, $\omega_{rms} \approx 2\Omega$ at $Ro = 1$. This effect is a likely cause for the reduced left-hand-side tail of the vorticity p.d.f. at $Ro = 1.44$ and $z = 0.5H$ in figure 9. There is considerable input of cyclonic vorticity at $Ro = 1$, but all negative vorticity is spread out, resulting in a positive skewness. For $Ro \ll 1$ the r.m.s. vorticity is smaller than 2Ω and anticyclonic vortices are stable; hence the distribution is more symmetric. For $Ro \gg 1$ there is only marginal preference for cyclonic vorticity. Indeed, the situation of unit Rossby number appears to be a special case.

Closer to the top plate ($z = 0.8H$, triangles in figure 11) the skewness is generally larger than in the centre ($z = 0.5H$, squares in figure 11). At Rossby numbers larger than about 0.5 there is reasonable quantitative agreement between results from experiment and simulation. For $Ro \lesssim 0.5$, however, the results at $z = 0.8H$ diverge: a rather constant $S_{\omega_z} \approx 0.25$ is found in the experiments, while the numerical S_{ω_z} reaches values up to 1.6. The experimental results are similar to those of Vorobieff & Ecke (2002). They mentioned the trend of the vorticity distribution becoming more symmetric as the Rossby number decreased below 0.3. This effect is absent in the simulation results at height $z = 0.8H$. We cannot fully explain the discrepancy yet, but it is expected that at least part of it is due to the aforementioned differences in resolution. We also note that calculation of skewness requires a third-order power of vorticity, which magnifies any finite-difference errors considerably.

5.3. *Correlation of vertical velocity and vertical vorticity*

In Kunnen *et al.* (2008*b*) we investigated the relation between the measured vertical velocity w and the vertical vorticity ω_z by plotting the p.d.f.s of the product $w\omega_z$. The resulting distributions are of so-called stretched-exponential shape and have even more pronounced tails than an exponential distribution. The skewness of these distributions can be used to quantify the correlation between the two variables w and ω_z. We showed in Kunnen *et al.* (2008*b*) that in the central region at $z = 0.5H$ the skewness $S_{w\omega_z}$ remains close to zero, indicating that w and ω_z are not correlated at

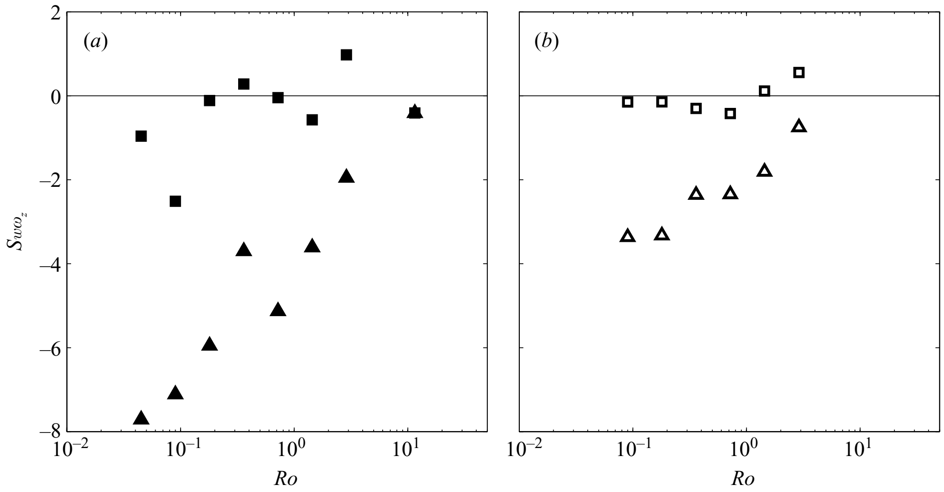

FIGURE 12. Skewness of the distributions of $w\omega_z$ as a function of Ro. Included are the heights $z=0.5H$ (squares) and $z=0.8H$ (triangles): (*a*) current numerical results; (*b*) experimental results originally presented in Kunnen *et al.* (2008*b*).

that height. Conversely, at the other measurement position $z=0.8H$ a pronounced negative skewness was found under rotation, which increased in magnitude as the Rossby number was decreased. Thus close to the top plate positive vertical vorticity is correlated with negative vertical velocity and vice versa. The correlation is another sign pointing to the formation of the vortical plumes near the top plate.

A similar analysis is performed for the simulation results. The skewness $S_{w\omega_z}$ is presented in figure 12(*a*) for several Ro values at $z=0.5H$ and $0.8H$. The previous experimental results from Kunnen *et al.* (2008*b*) are also included (figure 12*b*). The numerical values of the skewness are larger than those found in the experiment, but the same trends are found. Quantitative discrepancies between experiment and simulation are accumulated differences from the velocity and vorticity statistics. At $z=0.8H$ the skewness becomes a large negative value for smaller Rossby numbers. At $z=0.5H$ it does not show much variation with Ro. Thus the preferred coupling of negative w and positive ω_z (and vice versa) at the off-centre position $z=0.8H$ is also readily observed in the simulations. We have validated that near the bottom plate the preferred coupling is of positive w and positive ω_z or negative w and negative ω_z.

5.4. *Temperature statistics*

The p.d.f. of temperature was an important ingredient in the discovery of the ‘hard’ turbulent state in non-rotating convection (Heslot, Castaing & Libchaber 1987; Castaing *et al.* 1989). It was found that at Rayleigh numbers above a certain critical value (in the cited experiments in helium, $Ra_c \approx 4\times 10^7$) the temperature p.d.f. changed from Gaussian to exponential. This transition is ascribed to a change in the plume release in the boundary layers (Castaing *et al.* 1989). Above the critical Ra value the release of plumes from the boundary layers is highly intermittent, generating localized bursts of strong temperature contrast, differing from a smoother plume structure with Gaussian temperature statistics below the critical value. Exponential temperature p.d.f.s at high Rayleigh numbers have also been measured in water ($\sigma \approx 5$) by Solomon & Gollub (1990) and in mercury ($\sigma \approx 0.02$) by Glazier *et al.* (1999).

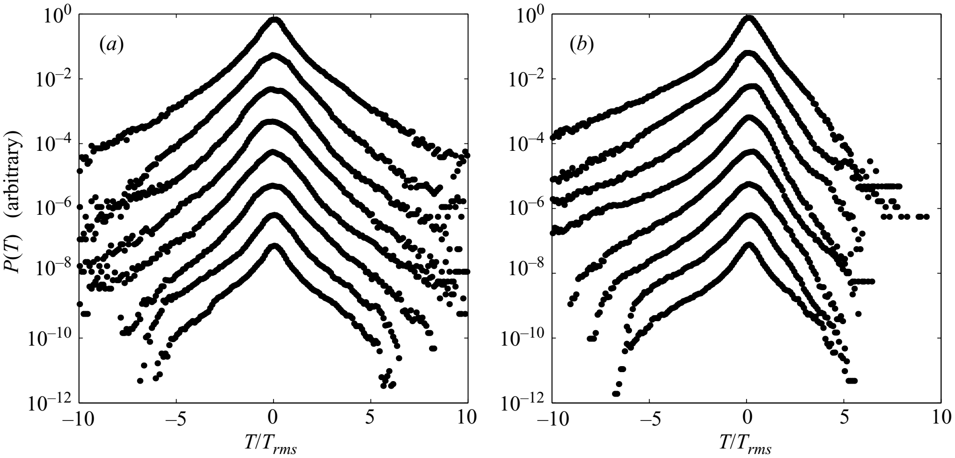

FIGURE 13. Temperature p.d.f.s at (*a*) $z = 0.5H$ and (*b*) $z = 0.8H$. From top to bottom the corresponding Rossby numbers are $Ro = 11.52$, 2.88, 1.44, 0.72, 0.36, 0.18, 0.090 and 0.045. The curves are shifted downward by intervals of one decade for clarity.

For convection with rotation these p.d.f.s have also been investigated. In simulations at $\sigma = 1$ and various Rayleigh numbers up to $Ra = 1.8 \times 10^8$ at constant $Ro = 0.75$ the p.d.f.s remain Gaussian (Julien *et al.* 1996*b*). In experiments at $\sigma = 6.3$, for Ra values up to 5×10^8 and in the range $0.1 \leqslant Ro \leqslant 1.5$, Liu & Ecke (1997) observed only exponential p.d.f.s. In contrast, experiments by Hart *et al.* (2002) at $\sigma = 8.4$ and at even higher Rayleigh number $Ra \approx 3 \times 10^{11}$ displayed Gaussian statistics at $Ro = 6$.

Temperature p.d.f.s have been calculated from the numerical probe data. (Since no temperature measurement has been carried out we only present simulation results concerning temperature statistics.) In figure 13(*a*) the p.d.f.s, at $z = 0.5H$, are shown for $0.045 \leqslant Ro \leqslant 11.52$. It is found that our simulations fully confirm the findings of Liu & Ecke (1997): in all cases exponential distributions are found. At the lowest Rossby numbers the tails of the p.d.f.s on both sides in figure 13(*a*) and the left-hand-side tails of the p.d.f.s in figure 13(*b*) drop off abruptly. This is caused by an increased T_{rms} at these Ro (figure 4), which is used to scale the horizontal axis, in combination with the simultaneous requirement that the temperature should always remain in the range $0 \leqslant T \leqslant 1$. The probability for the temperature to attain values approaching either 0 or 1 diminishes rapidly, hence the drop-off.

The same plots for height $z = 0.8H$ in figure 13(*b*) reveal a remarkable uniformity. The p.d.f.s are skewed negatively. As the measurement is taken closer to the top plate, plumes with lower-than-average temperatures are more probable, hence the stronger negative tail. The shapes at all Ro considered here are very similar. For the lowest Ro again the confinement of $0 \leqslant T \leqslant 1$ is observed, reducing the skewness magnitude. Quantitatively, $S \approx -2$ for Rossby numbers equal to 0.72 and higher, while for the lower Rossby numbers S decreases in magnitude with decreasing Ro to $S \approx -1$ at $Ro = 0.045$.

Since the parameter range for these numerical simulations is comparable to that used by Liu & Ecke (1997), it is not surprising that the exponential p.d.f.s are found here as well. The intense temperature fluctuations in rotating convection are thus predominantly associated with the presence of confined coherent structures, namely the vortical plumes. The transition from the plumes of non-rotating convection to the

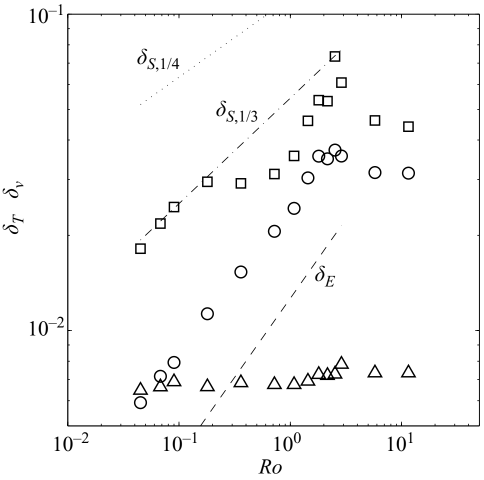

FIGURE 14. Boundary layers in cylindrical rotating convection. The following are included: dimensionless thermal-boundary-layer thickness δ_T near horizontal plates (triangles) and dimensionless viscous-boundary-layer thickness δ_ν near horizontal plates (circles) and near the sidewall (squares). Dimensionless boundary-layer scales $\delta_E = Ek^{1/2}$ (Ekman layer at bottom and top plates), $\delta_{S,1/3} = Ek^{1/3}$ and $\delta_{S,1/4} = Ek^{1/4}$ (inner and outer Stewartson layer at sidewall, respectively) are also included.

vortical tube-like structures of rotating convection apparently has no effect on the shape of the temperature p.d.f.

6. Boundary layers and mean temperature gradient

In this section we treat two results that are only available from the simulations: the boundary layers near the plates and the sidewall and the mean temperature gradient found in the fluid bulk. The experimental arrangement in its current configuration did not allow for an investigation of the boundary-layer regions.

6.1. *Boundary-layer thicknesses*

Viscous boundary layers are formed near both horizontal plates and near the sidewall. Thermal boundary layers are only found near the horizontal plates, as the sidewall is adiabatic. Under rotation the boundary layers are active: fluid exchange between boundary layer and bulk takes place because of Ekman pumping and/or suction. The thickness of the boundary layer is important for the magnitude of these fluxes. The active nature of the boundary layers makes them an integral part of the description of turbulent rotating convection. Here we present simulation results on the thicknesses of the various boundary layers.

A commonly applied definition of the boundary-layer size is the distance to the wall of the maximum in the r.m.s. velocity or temperature. This definition has been used to find boundary-layer scales near the horizontal plates (from the azimuthal-velocity r.m.s. profile and r.m.s. temperature profile close to the cylinder axis) and near the sidewall (from the azimuthally averaged vertical-velocity r.m.s. profile in radial direction at mid-height). These are presented for the various *Ro* in figure 14.

The thermal-boundary-layer thickness δ_T is nearly independent of *Ro*. It is buried within the thicker viscous layer of thickness δ_ν since $\sigma > 1$. Rotation exclusively affects the viscous boundary layer directly; any changes to the thermal boundary layer are caused indirectly. Only at the lowest Ro considered here the viscous boundary layer is thinner than the thermal layer. Then the bulk flow field can directly affect the thermal layer; at even lower Ro a change of its thickness is expected. The viscous-boundary-layer thickness near the horizontal plates rises with increasing Ro up to $Ro \approx 2$. Its slope matches well with the dimensionless Ekman-layer thickness $\delta_E = Ek^{1/2} \sim Ta^{-1/4} \sim Ro^{1/2}$ (the Ekman number is $Ek \equiv \nu/(\Omega H^2) = \sqrt{4/Ta}$; Ekman 1905), but quantitatively it is roughly larger by the factor two.

The viscous layer on the sidewall shows more changes under rotation. At the lowest $Ro \lesssim 0.2$ considered, the thickness follows the (dimensionless) thickness of the inner Stewartson layer $\delta_{S,1/3} = Ek^{1/3} \sim Ro^{1/3}$ (Stewartson 1957). The outer Stewartson layer $\delta_{S,1/4} = Ek^{1/4} \sim Ro^{1/4}$ is also included for reference. Around $Ro \approx 2$ there is a considerable widening, as the LSC is rather unstable at this Ro. The layer thickness for $Ro \gtrsim 3$ is unaffected by rotation.

6.2. *Mean temperature gradient*

In non-rotating convection the vertical mean temperature profile can be divided into three regions: a well-mixed isothermal (convective) bulk, with two (conductive) boundary-layer regions of dimensionless thickness $\delta_T = 1/(2Nu)$ (Busse 1978; Grossmann & Lohse 2000). When rotation is added a mean temperature gradient persists over the fluid bulk (Julien *et al.* 1996*b*; Hart & Ohlsen 1999). Measurements in air-cooled rotating convection without a solid top plate also indicated the presence of a mean gradient (Boubnov & Golitsyn 1990; Fernando *et al.* 1991). According to Julien *et al.* (1996*b*) the presence of the gradient can be seen as an indication that the vertical mixing is less efficient than in the non-rotating case.

In the current simulations the mean temperature is averaged in time at the cylinder axis. Next, the mean gradient is calculated at the mid-height $z = 0.5$ by fitting a linear function for $0.3 < z < 0.7$. The strength of the mean gradient and its dependence on Ro is depicted in figure 15. At high Ro, i.e. $Ro \gtrsim 2.5$, a small positive gradient is found. This is explained by the overturning motion of the LSC. Warm plumes rise on one side of the cylinder and then cross horizontally in the upper half of the cylinder. Cold plumes cross the cell in the opposite fashion. On the axis a small positive gradient may be found. This gradient has been measured before by Tilgner, Belmonte & Libchaber (1993) and Brown & Ahlers (2007), both for non-rotating convection in water. Tilgner *et al.* (1993) measured a dimensionless gradient $\partial \langle T \rangle / \partial z = 0.020 \pm 0.007$ at $Ra = 1.1 \times 10^9$ and $\sigma = 6.6$. Brown & Ahlers (2007) measured the gradient in a range of Rayleigh numbers at two Prandtl numbers $\sigma = 4.4$ and 5.5. At $Ra = 1.0 \times 10^9$ and $\sigma = 5.5$ the corresponding gradient is $\partial \langle T \rangle / \partial z = 0.015$. These values are quantitatively in good agreement with the gradient found in our simulations at $Ro = 5.76$, but the value at $Ro = 11.52$ is found to be lower. A reconsideration of our simulation run at $Ro = \infty$ (Kunnen *et al.* 2008*a*) provided the gradient value $\partial \langle T \rangle / \partial z = 0.0145 \pm 0.0004$, consistent with the aforementioned experimental results.

At smaller Rossby numbers $Ro \lesssim 2.5$ a mean negative gradient persists. A qualitative description of the observation of a mean temperature gradient in rotating convection is given by Julien *et al.* (1996*b*, 1999), Legg *et al.* (2001) and Sprague *et al.* (2006). They postulated that the merger of vortical plumes, reported in many studies (Boubnov & Golitsyn 1986; Zhong *et al.* 1993; Julien *et al.* 1996*b*; Ecke & Liu 1998; Sprague *et al.* 2006), enhances horizontal mixing of the temperature anomaly of the plumes, which results in a mean temperature gradient.

Several regimes can be discerned in the mean temperature gradient plot as a function of Ro, below $Ro = 2.5$. In the range $1 \lesssim Ro \lesssim 2.5$ the dependence on Ro is

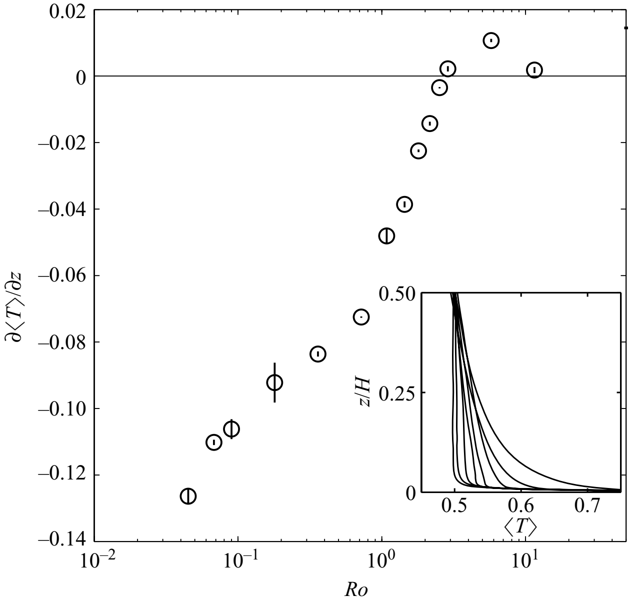

FIGURE 15. Mean temperature gradient $\partial\langle T\rangle/\partial z$ at mid-height along the axis of the cylinder as a function of Ro. Error margins are indicated by vertical lines in the symbols. The inset contains the mean temperature profile at the cylinder axis for the bottom half of the domain. From left to right the corresponding Rossby numbers are $Ro = 5.76$, 2.88, 1.44, 0.72, 0.36, 0.18, 0.09 and 0.045.

stronger than for $0.1 \lesssim Ro \lesssim 1$. At the lowest $Ro \lesssim 0.1$ there is again a steeper slope. When the Rossby number is decreased even further, eventually the gradient must approach the conductive value $\partial\langle T\rangle/\partial z = -1$ throughout the fluid. All fluid motions are then inhibited by rotation, and the only heat transfer is due to conduction, for which $Nu = 1$ by definition.

7. Anisotropy

Just as in our previous experimental work (Kunnen *et al.* 2008*b*), we can consider the anisotropy of the simulated flow with the invariants of the anisotropy tensor and the Lumley map (Lumley & Newman 1977; Lumley 1978; Choi & Lumley 2001; Simonsen & Krogstad 2005).

The Reynolds stress tensor is defined as $R_{ij} \equiv \overline{u_i u_j}$. Here u_i is the ith Cartesian velocity component (i and j take integer values 1–3; here 3 is taken as the vertical direction), and the overbar indicates spatial averaging, which in this case is applied over the line segment with the numerical probes (see § 3.1). It has been validated that in this spatial extent the flow is homogeneous, such that spatial averaging is equivalent to averaging in time. Closer to the sidewall stronger inhomogeneities occur.

The anisotropy of the flow can be characterized with $b_{ij} \equiv R_{ij}/R_{kk} - (1/3)\delta_{ij}$, the deviatoric part of R_{ij}; δ_{ij} is the second-order Kronecker tensor, and summation over repeated indices is implied; b_{ij} is a symmetric, traceless tensor. The first invariant of b_{ij} (the trace) is thus zero. The second and third invariants of b_{ij}, denoted here as II and III, are

$$II \equiv -b_{ij}b_{ji}/2, \quad III \equiv b_{ij}b_{jk}b_{ki}/3 = \det(b_{ij}). \tag{7.1}$$

The invariants provide a means of graphical evaluation of the anisotropy (Lumley & Newman 1977; Lumley 1978; Choi & Lumley 2001; Simonsen & Krogstad 2005). All turbulent states that can be realized are found within a triangular region in the $(III, -II)$ plane or the so-called Lumley triangle (see e.g. figure 1 of Simonsen & Krogstad 2005 and figure 16 of this work). Three limiting cases are found in the corners: three-component isotropic turbulence is found for $II = III = 0$; two-component axisymmetric turbulence is found in the left corner of the triangle; the right corner is the limiting case of one-component turbulence. The line between the left and right extreme points represents non-axisymmetric two-component turbulence. The limiting curve that connects the origin to the leftmost point was designated pancake-shaped turbulence by Choi & Lumley (2001) and disk-like turbulence by Simonsen & Krogstad (2005): b_{ij} possesses one small and two large eigenvalues, so that one component of the turbulent kinetic energy is smaller than the other two. The curve from the origin to the rightmost point represents the state in which b_{ij} has one eigenvalue that is larger than the other two, designated cigar-shaped turbulence by Choi & Lumley (2001) and rod-like turbulence by Simonsen & Krogstad (2005).

In our previous work (Kunnen *et al.* 2008*b*) it was found that rotation affects the turbulence anisotropy tensor differently in various positions inside the cylinder. In the central region the tensor has one dominant eigenvalue, pointing out that velocity fluctuations in one direction (vertical) are dominant. Closer to the top plate a remarkably isotropic state is found, where the velocity fluctuations in the three spatial directions are of roughly equal strength. This behaviour is remarkably different from rotating turbulence (van Bokhoven 2007), where rotation causes the anisotropy tensor to develop two large eigenvalues and horizontal velocity is strongest.

The invariants of the anisotropy tensor can also be calculated from the time series of velocity components, obtained from the numerical probes at positions $z = 0.5H$ and $z = 0.8H$. In figure 16 Lumley maps at representative Ro values are shown, with the temporal evolution of the invariants II and III. At $Ro = 11.52$ there is a lot of spread in time for the invariants, at both heights. When the Rossby number is decreased distinct trends are observed at the two heights. At mid-height the trajectory is increasingly pressed against the limiting curve for axisymmetric turbulence with one large eigenvalue. This again points at the development of the columnar vortical plumes under rotation. At $z = 0.8H$ a reduction in the spread of the trajectory is observed: it is confined to a smaller area near the origin of the graph (the point that designates three-component isotropic turbulence). Thus at this height the turbulence becomes increasingly isotropic as Ro is reduced.

A concise view of the dependence on rotation of the invariants is obtained by taking the time-averaged values and plotting the time averages in a Lumley triangle. This plot is shown in figure 17. Included are the following Rossby numbers: $Ro = 11.52$, 2.88, 1.44, 0.72, 0.36, 0.18, 0.09, 0.068 and 0.045. The path that belongs to $z = 0.5H$ (filled triangles) shows no clear uniform direction for the higher Rossby numbers, $Ro > 1$. At lower Ro the path goes downward up to the point for $Ro = 0.18$, the point closest to the isotropic state in this path. For the lowest $Ro < 0.18$ the path follows the bounding curve upward, which indicates the growing anisotropy as one eigenvalue of the anisotropy tensor (the one corresponding to vertical velocity fluctuations) becomes larger relative to the other two. The path at $z = 0.8H$ nearly uniformly approaches the point of isotropy at the origin.

Qualitatively the paths in the Lumley triangle from experiment and simulation are very similar. Only quantitatively there is some discrepancy. The measured velocity fluctuations in the experiments are lower than found in the simulations. The stronger

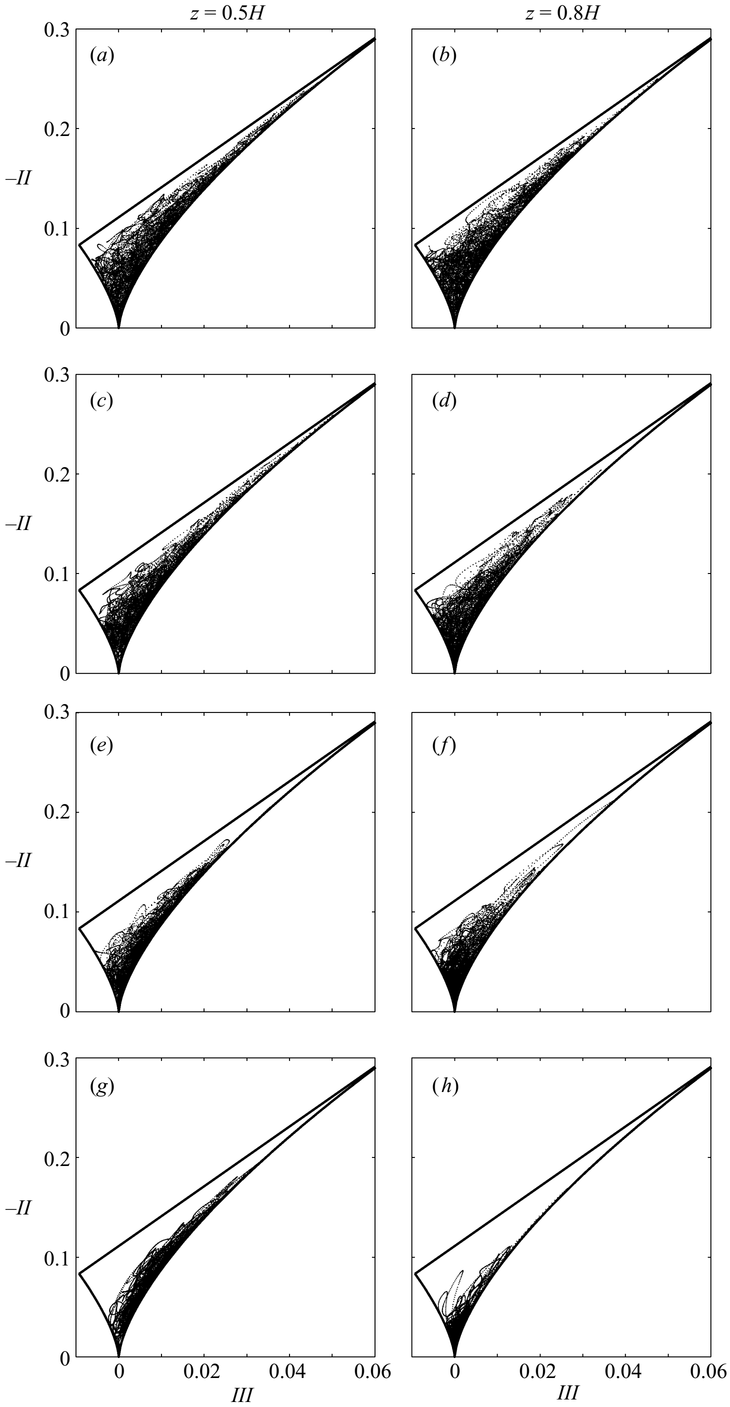

FIGURE 16. Temporal evolution of the invariants II and III at selected Rossby numbers: (*a*, *b*) $Ro = 11.52$, (*c*, *d*) $Ro = 1.44$, (*e*, *f*) $Ro = 0.36$, (*g*, *h*) $Ro = 0.045$. Two vertical positions are included (*a*, *c*, *e*, *g*) at $z = 0.5H$ and (*b*, *d*, *f*, *h*) at $z = 0.8H$. The thick grey lines are the boundaries of the Lumley triangle.

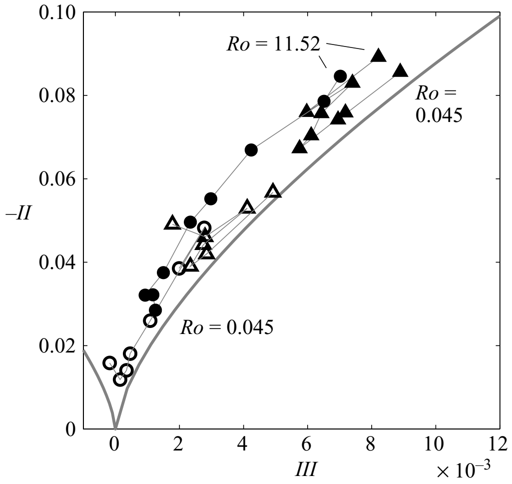

FIGURE 17. Positions in the Lumley triangle of the time-averaged invariants $\langle II \rangle$ and $\langle III \rangle$ for Rossby numbers 11.52, 2.88, 1.44, 0.72, 0.36, 0.18, 0.09, 0.068 and 0.045. The circles are for $z = 0.8H$ and the triangles for $z = 0.5H$. The thick grey lines bound the Lumley triangle. Filled symbols: current numerical data. Open symbols: experimental data taken from Kunnen *et al.* (2008*b*).

fluctuations from the simulations (and corresponding stronger excursions of the trajectories in the maps of figure 16) translate to larger numerical mean values for the invariants in the simulation results. Another difference is that the excursion towards the negative side of $\langle III \rangle$, towards pancake-shaped or disk-like turbulence, found in the experiment at $z = 0.8H$ for the lowest $Ro = 0.09$, is not reproduced in the simulations. It may well be that at even lower Ro such a development is also observed in the simulations.

8. Conclusions

The effects of rotation on many aspects of turbulent rotating convection have been discussed based on results from measurements of flow velocity and DNSs. A tentative separation into three regimes based on the Rossby number is suggested below.

(*i*) $Ro \gtrsim 2$. In this range of Rossby numbers the flow behaviour is dominated by the presence of the LSC. Variation of Ro has only minor effect. There is an increase found in the r.m.s. velocity and vorticity fluctuations for $Ro \lesssim 3$ compared with $Ro \gtrsim 3$, which we suspect is a sign of the Ekman pumping mechanism becoming active. Additionally, this Rossby number marks the point at which rotation influences the strength and stability of the LSC as shown in Kunnen *et al.* (2008*a*). In distribution functions of the vertical vorticity some slight asymmetry is found, pointing at a preference for cyclonic vorticity induced by the Ekman pumping even for modest rotation rates.

(*ii*) $0.1 \lesssim Ro \lesssim 2$. The LSC is replaced by vortical columns as the dominant flow structure. The viscous boundary layers at the bottom and top plates and the sidewall follow the scalings of the boundary-layer thicknesses of laminar rotating flow, viz. the Ekman and inner Stewartson layers. In this range the turbulence intensity drops as rotation is increased approximately as a power law, $Ro^{0.2}$. Conversely, the vorticity fluctuations in the centre are hardly affected by rotation, while closer to the plates they grow in magnitude as rotation is increased. The temperature r.m.s. values show an opposite and stronger relation with Ro than the r.m.s. velocities: they scale approximately as $Ro^{-0.32}$. A mean vertical temperature gradient is found in the bulk fluid, in contrast with the well-mixed interior found in non-rotating convection. In spite of these signs of stabilization the convective heat flux, the Nusselt number, is larger than without rotation (Rossby 1969; Liu & Ecke 1997; Kunnen *et al.* 2008*a*; Zhong *et al.* 2009).

(*iii*) $Ro \lesssim 0.1$. In this range of Rossby numbers rotation has a more pronounced influence on the turbulence intensities, including vorticity: a considerably steeper dependence on Ro is reported in this range. The stabilizing effect of rotation is clearly demonstrated in these statistics. The anisotropy in the flow reaches opposite extremes: in the centre a clear anisotropy is found, where one velocity component is dominant, while closer to the plates a transition towards the isotropic state is observed.

The division into three regimes matches with the classification by Boubnov & Golitsyn (1990, 1995): these authors label the first regime 'thermal turbulence', the second regime 'irregular geostrophic turbulence' and the last regime '(quasi-)regular vortex grid.'

This combined numerical and experimental investigation of the intricate and highly relevant problem that is turbulent rotating convection has provided us with a clear overview of the turbulence statistics. It has also become clear that the coherent vortical plumes that are found in this flow play an important role. Therefore we are now investigating these structures in more detail.

The authors wish to thank Laurens van Bokhoven (SPIV algorithm and design of the rotating table) and Rinie Akkermans (SPIV algorithm) as well as Ad Holten, Gerald Oerlemans and Freek van Uittert (design and manufacturing of the experimental set-up) for their contributions to this work. R.P.J.K. wishes to thank the Foundation for Fundamental Research on Matter (Stichting voor Fundamenteel Onderzoek der Materie, FOM) for financial support. This work was sponsored by the National Computing Facilities Foundation (NCF) for the use of supercomputer facilities, with financial support from the Netherlands Organisation for Scientific Research (NWO).

REFERENCES

Ahlers, G., Grossmann, S. & Lohse, D. 2009 Heat transfer and large-scale dynamics in turbulent Rayleigh–Bénard convection. *Rev. Mod. Phys.* **81**, 503–537.

Ashkenazi, S. & Steinberg, V. 1999 Spectra and statistics of velocity and temperature fluctuations in turbulent convection. *Phys. Rev. Lett.* **83**, 4760–4763.

Balachandar, S. & Sirovich, L. 1991 Probability distribution functions in turbulent convection. *Phys. Fluids* A **3**, 919–927.

van Bokhoven, L. J. A. 2007 Experiments on rapidly rotating turbulent flows. PhD thesis, Eindhoven University of Technology, Eindhoven, The Netherlands.

van Bokhoven, L. J. A., Clercx, H. J. H., van Heijst, G. J. F. & Trieling, R. R. 2009 Experiments on rapidly rotating turbulent flows. *Phys. Fluids* **21**, 096601.

Boubnov, B. M. & Golitsyn, G. S. 1986 Experimental study of convective structures in rotating fluids. *J. Fluid Mech.* **167**, 503–531.

Boubnov, B. M. & Golitsyn, G. S. 1990 Temperature and velocity field regimes of convective motions in a rotating plane fluid layer. *J. Fluid Mech.* **219**, 215–239.

Boubnov, B. M. & Golitsyn, G. S. 1995 *Convection in Rotating Fluids*. Kluwer Academic.

Brown, E. & Ahlers, G. 2006 Effect of the Earth's Coriolis force on the large-scale circulation of turbulent Rayleigh–Bénard convection. *Phys. Fluids* **18**, 125108.

Brown, E. & Ahlers, G. 2007 Temperature gradients, and search for non-Boussinesq effects, in the interior of turbulent Rayleigh–Bénard convection. *Europhys. Lett.* **80**, 14001.

Busse, F. H. 1978 Non-linear properties of thermal convection. *Rep. Progr. Phys.* **41**, 1929–1967.

Busse, F. H. 1994 Convection driven zonal flows and vortices in the major planets. *Chaos* **4**, 123–134.

Busse, F. H. & Carrigan, C. R. 1976 Laboratory simulation of thermal convection in rotating planets and stars. *Science* **191**, 81–83.

Camussi, R. & Verzicco, R. 2004 Temporal statistics in high Rayleigh number convective turbulence. *Eur. J. Mech.* B **23**, 427–442.

Castaing, B., Gagne, Y. & Hopfinger, E. J. 1990 Velocity probability density functions of high Reynolds number turbulence. *Physica* D **46**, 177–200.

Castaing, B., Gunaratne, G., Heslot, F., Kadanoff, L., Libchaber, A., Thomae, S., Wu, X.-Z., Zaleski, S. & Zanetti, G. 1989 Scaling of hard thermal turbulence in Rayleigh–Bénard convection. *J. Fluid Mech.* **204**, 1–30.

Chandrasekhar, S. 1953 The instability of a layer of fluid heated from below and subject to Coriolis forces. *Proc. R. Soc. Lond.* A **217**, 306–327.

Chandrasekhar, S. 1961 *Hydrodynamic and Hydromagnetic Stability*. Oxford University Press.

Choi, K.-S. & Lumley, J. L. 2001 The return to isotropy of homogeneous turbulence. *J. Fluid Mech.* **436**, 59–84.

Ecke, R. E. & Liu, Y. 1998 Traveling-wave and vortex states in rotating Rayleigh–Bénard convection. *Intl J. Engng Sci.* **36**, 1471–1480.

Ekman, V. W. 1905 On the influence of the Earth's rotation on ocean-currents. *Arch. Math. Astron. Phys.* **2**, 1–52.

Fernando, H. J. S., Chen, R.-R. & Boyer, D. L. 1991 Effects of rotation on convective turbulence. *J. Fluid Mech.* **228**, 513–547.

Gascard, J.-C., Watson, A. J., Messias, M.-J., Olsson, K. A., Johannessen, T. & Simonsen, K. 2002 Long-lived vortices as a mode of deep ventilation in the Greenland Sea. *Nature (Lond.)* **416**, 525–527.

Gill, A. E. 1982 *Atmosphere–Ocean Dynamics*. Academic.

Glazier, J. A., Segawa, T., Naert, A. & Sano, M. 1999 Evidence against 'ultrahard' thermal turbulence at very high Rayleigh numbers. *Nature (Lond.)* **398**, 307–310.

Goldstein, H. F., Knobloch, E., Mercader, I. & Net, M. 1993 Convection in a rotating cylinder. Part 1. Linear theory for moderate Prandtl numbers. *J. Fluid Mech.* **248**, 583–604.

Grossmann, S. & Lohse, D. 2000 Scaling in thermal convection: a unifying theory. *J. Fluid Mech.* **407**, 27–56.

Hart, J. E. 2000 On the influence of centrifugal buoyancy on rotating convection. *J. Fluid Mech.* **403**, 133–151.

Hart, J. E., Kittelman, S. & Ohlsen, D. R. 2002 Mean flow precession and temperature probability density functions in turbulent rotating convection. *Phys. Fluids* **14**, 955–962.

Hart, J. E. & Ohlsen, D. R. 1999 On the thermal offset in turbulent rotating convection. *Phys. Fluids* **11**, 2101–2107.

Heslot, F., Castaing, B. & Libchaber, A. 1987 Transition to turbulence in helium gas. *Phys. Rev.* A **36**, 5870–5873.

Jones, C. A. 2000 Convection-driven geodynamo models. *Phil. Trans. R. Soc. Lond.* A **358**, 873–897.

Julien, K., Legg, S., McWilliams, J. & Werne, J. 1996*a* Hard turbulence in rotating Rayleigh–Bénard convection. *Phys. Rev.* E **53**, R5557–R5560.

Julien, K., Legg, S., McWilliams, J. & Werne, J. 1996*b* Rapidly rotating turbulent Rayleigh–Bénard convection. *J. Fluid Mech.* **322**, 243–273.

Julien, K., Legg, S., McWilliams, J. & Werne, J. 1999 Plumes in rotating convection. Part 1. Ensemble statistics and dynamical balances. *J. Fluid Mech.* **391**, 151–187.

Kerr, R. M. 1996 Rayleigh number scaling in numerical convection. *J. Fluid Mech.* **310**, 139–179.

Kerr, R. M. & Herring, J. R. 2000 Prandtl number dependence of Nusselt number in direct numerical simulations. *J. Fluid Mech.* **419**, 325–344.

van de Konijnenberg, J. A., Andersson, H. I., Billdal, J. T. & van Heijst, G. J. F. 1994 Spin-up in a rectangular tank with low angular velocity. *Phys. Fluids* **6**, 1168–1176.

Krishnamurti, R. & Howard, L. N. 1981 Large-scale flow generation in turbulent convection. *Proc. Natl. Acad. Sci. USA* **78**, 1981–1985.

Kunnen, R. P. J. 2008 Turbulent rotating convection. PhD thesis, Eindhoven University of Technology, Eindhoven, The Netherlands.

Kunnen, R. P. J., Clercx, H. J. H. & Geurts, B. J. 2006 Heat flux intensification by vortical flow localization in rotating convection. *Phys. Rev.* E **74**, 056306.

Kunnen, R. P. J., Clercx, H. J. H. & Geurts, B. J. 2008*a* Breakdown of large-scale circulation in turbulent rotating convection. *Europhys. Lett.* **84**, 24001.

Kunnen, R. P. J., Clercx, H. J. H. & Geurts, B. J. 2008*b* Enhanced vertical inhomogeneity in turbulent rotating convection. *Phys. Rev. Lett.* **101**, 174501.

Kunnen, R. P. J., Clercx, H. J. H., Geurts, B. J., van Bokhoven, L. J. A., Akkermans, R. A. D. & Verzicco, R. 2008*c* Numerical and experimental investigation of structure function scaling in turbulent Rayleigh–Bénard convection. *Phys. Rev.* E **77**, 016302.

Kunnen, R. P. J., Geurts, B. J. & Clercx, H. J. H. 2009 Turbulence statistics and energy budget in rotating Rayleigh–Bénard convection. *Eur. J. Mech.* B **28**, 578–589.

Küppers, G. & Lortz, D. 1969 Transition from laminar convection to thermal turbulence in a rotating fluid layer. *J. Fluid Mech.* **35**, 609–620.

Legg, S., Julien, K., McWilliams, J. & Werne, J. 2001 Vertical transport by convection plumes: modification by rotation. *Phys. Chem. Earth* B **26**, 259–262.

Lide, D. R. (Ed.) 2007–2008 *CRC Handbook of Chemistry and Physics*, 88th edn. CRC Press/Taylor and Francis.

Liu, Y. & Ecke, R. E. 1997 Heat transport scaling in turbulent Rayleigh–Bénard convection: effects of rotation and Prandtl number. *Phys. Rev. Lett.* **79**, 2257–2260.

Lucas, P. G. J., Pfotenhauer, J. M. & Donnelly, R. J. 1983 Stability and heat transfer of rotating cryogens. Part 1. Influence of rotation on the onset of convection in liquid ^{4}He. *J. Fluid Mech.* **129**, 251–264.

Lumley, J. L. 1978 Computational modelling of turbulent flows. *Adv. Appl. Mech.* **18**, 123–175.

Lumley, J. L. & Newman, G. R. 1977 The return to isotropy of homogeneous turbulence. *J. Fluid Mech.* **82**, 161–178.

Marshall, J. & Schott, F. 1999 Open-ocean convection: observations, theory, and models. *Rev. Geophys.* **37**, 1–64.

Miesch, M. S. 2000 The coupling of solar convection and rotation. *Solar Phys.* **192**, 59–89.

Moeng, C.-H. & Rotunno, R. 1990 Vertical-velocity skewness in the buoyancy-driven boundary layer. *J. Atmos. Sci.* **47**, 1149–1162.

Nakagawa, Y. & Frenzen, P. 1955 A theoretical and experimental study of cellular convection in rotating fluids. *Tellus* **7**, 1–21.

Oresta, P., Stringano, G. & Verzicco, R. 2007 Transitional regimes and rotation effects in Rayleigh–Bénard convection in a slender cylindrical cell. *Eur. J. Mech.* B **26**, 1–14.

Pedlosky, J. 1987 *Geophysical Fluid Dynamics*, 2nd edn. Springer.

Pfotenhauer, J. M., Lucas, P. G. J. & Donnelly, R. J. 1984 Stability and heat transfer of rotating cryogens. Part 2. Effects of rotation on heat-transfer properties of convection in liquid ^{4}He. *J. Fluid Mech.* **145**, 239–252.

Pfotenhauer, J. M., Niemela, J. J. & Donnelly, R. J. 1987 Stability and heat transfer of rotating cryogens. Part 3. Effects of finite cylindrical geometry and rotation on the onset of convection. *J. Fluid Mech.* **175**, 85–96.

Prandtl, L. 1932 Meteorologische Anwendungen der Strömungslehre. *Beitr. Phys. Atmos.* **19**, 188–202.

Prasad, A. K. 2000 Stereoscopic particle image velocimetry. *Exp. Fluids* **29**, 103–116.

Qiu, X.-L., Shang, X.-D., Tong, P. & Xia, K.-Q. 2004 Velocity oscillations in turbulent Rayleigh–Bénard convection. *Phys. Fluids* **16**, 412–423.

Qiu, X.-L. & Tong, P. 2001 Large-scale velocity structures in turbulent thermal convection. *Phys. Rev.* E **64**, 036304.

Raasch, S. & Etling, E. 1991 Numerical simulation of rotating turbulent thermal convection. *Beitr. Phys. Atmos.* **64**, 185–199.

Raffel, M., Willert, C. & Kompenhans, J. 1998 *Particle Image Velocimetry*. Springer.

Rogers, M. H. & Lance, G. N. 1960 The rotationally symmetric flow of a viscous fluid in the presence of an infinite rotating disk. *J. Fluid Mech.* **7**, 617–631.

Rossby, H. T. 1969 A study of Bénard convection with and without rotation. *J. Fluid Mech.* **36**, 309–335.

Sakai, S. 1997 The horizontal scale of rotating convection in the geostrophic regime. *J. Fluid Mech.* **333**, 85–95.

Shraiman, B. I. & Siggia, E. D. 1990 Heat transport in high-Rayleigh-number convection. *Phys. Rev.* A **42**, 3650–3653.

Siggia, E. D. 1994 High Rayleigh number convection. *Annu. Rev. Fluid Mech.* **26**, 137–168.

Simonsen, A. J. & Krogstad, P.-Å. 2005 Turbulent stress invariant analysis: clarification of existing terminology. *Phys. Fluids* **17**, 088103.

Solomon, T. H. & Gollub, J. P. 1990 Sheared boundary layers in turbulent Rayleigh–Bénard convection. *Phys. Rev. Lett.* **64**, 2382–2385.

Sprague, M., Julien, K., Knobloch, E. & Werne, J. 2006 Numerical simulation of an asymptotically reduced system for rotationally constrained convection. *J. Fluid Mech.* **551**, 141–174.

Stevens, R. J. A. M., Zhong, J.-Q., Clercx, H. J. H., Ahlers, G. & Lohse, D. 2009 Transitions between turbulent states in rotating Rayleigh–Bénard convection. *Phys. Rev. Lett.* **102**, 044502.

Stewartson, K. 1957 On almost rigid rotations. *J. Fluid Mech.* **3**, 17–26.

Tilgner, A., Belmonte, A. & Libchaber, A. 1993 Temperature and velocity profiles of turbulent convection in water. *Phys. Rev.* E **47**, R2253–R2256.

Verdoold, J., van Reeuwijk, M., Tummers, M. J., Jonker, H. J. J. & Hanjalić, K. 2008 Spectral analysis of boundary layers in Rayleigh–Bénard convection. *Phys. Rev.* E **77**, 016303.

Verzicco, R. & Camussi, R. 1997 Transitional regimes of low-Prandtl thermal convection in a cylindrical cell. *Phys. Fluids* **9**, 1287–1295.

Verzicco, R. & Camussi, R. 1999 Prandtl number effects in convective turbulence. *J. Fluid Mech.* **383**, 55–73.

Verzicco, R. & Camussi, R. 2003 Numerical experiments on strongly turbulent thermal convection in a slender cylindrical cell. *J. Fluid Mech.* **477**, 19–49.

Verzicco, R. & Orlandi, P. 1996 A finite-difference scheme for three-dimensional incompressible flow in cylindrical coordinates. *J. Comput. Phys.* **123**, 402–413.

Vorobieff, P. & Ecke, R. E. 1998*a* Transient states during spin-up of a Rayleigh–Bénard cell. *Phys. Fluids* **10**, 2525–2538.

Vorobieff, P. & Ecke, R. E. 1998*b* Vortex structure in rotating Rayleigh–Bénard convection. *Physica* D **123**, 153–160.

Vorobieff, P. & Ecke, R. E. 2002 Turbulent rotating convection: an experimental study. *J. Fluid Mech.* **458**, 191–218.

Xi, H.-D., Zhou, Q. & Xia, K.-Q. 2006 Azimuthal motion of the mean wind in turbulent thermal convection. *Phys. Rev.* E **73**, 056312.

Zhong, F., Ecke, R. E. & Steinberg, V. 1993 Rotating Rayleigh–Bénard convection: asymmetric modes and vortex states. *J. Fluid Mech.* **249**, 135–159.

Zhong, J.-Q., Stevens, R. J. A. M., Clercx, H. J. H., Verzicco, R., Lohse, D. & Ahlers, G. 2009 Prandtl-, Rayleigh-, and Rossby-number dependence of heat transport in turbulent rotating Rayleigh–Bénard convection. *Phys. Rev. Lett.* **102**, 044502.

Zhou, Q., Sun, C. & Xia, K.-Q. 2007 Morphological evolution of thermal plumes in turbulent Rayleigh–Bénard convection. *Phys. Rev. Lett.* **98**, 074501.